Spatiotemporal transcriptomic analyses reveal molecular gradient patterning during development and the tonotopic organization along the cochlear axis

Mengzhen Yan[1,2,#], Penghui Zhang[1,2,#], Yafan Wang[1,2,#], Haojie Wang[2,3,#], Junhong Li[4], Xiang Guo[5], Xiangyao Zeng[6], Zhili Feng[6], Yushan Gao[1,2], Fei Deng[7], Bicheng Zhu[1], Di Deng[4], Lu Ma[6], Yong Feng[6,8,9,10], Hua-Jun Wu[3,11,12,*], Yu Zhao[4,*] and Jun Li[1,*]

[1]Chengdu Institute of Biology, Chinese Academy of Sciences, Chengdu 610213, China

[2]University of Chinese Academy of Sciences, Beijing, China.

[3]Key Laboratory of Carcinogenesis and Translational Research (Ministry of Education/Beijing), Peking University Cancer Hospital and Institute, Beijing100142, China.

[4]Department of Otolaryngology-Head & Neck Surgery, West China Hospital, Sichuan University, Chengdu 610041, China

[5]Institute of Blood Diseases, Department of Hematology, Sichuan Academy of Medical Sciences & Sichuan Provincial People's Hospital, School of Medicine of University of Electronic Science and Technology of China, Sichuan, Chengdu 610000, China.

[6]Institute of Cytology and Genetics, Hengyang Medical School, University of South China, Hengyang 421000, China

[7]Graduate School of Biomedical Engineering, Faculty of Engineering, University of New South Wales, Sydney 2052, Australia

[8]Department of Otorhinolaryngology, The Affiliated Changsha Central Hospital, Hengyang Medical School, University of South China, Changsha 410028, China

[9]Institute of Otorhinolaryngology, Head and Neck Surgery, University of South China,

Changsha 410028, China

[10]MOE Key Lab of Rare Pediatric Diseases & Institute for Future Sciences, University of South China, Changsha 410008, China

[11]Department of Biomedical Informatics, School of Basic Medical Sciences, Peking University Health Science Center, Beijing 100191, China.

[12]Center for Precision Medicine Multi-Omics Research, Institute of Advanced Clinical Medicine, Peking University, Beijing 100191, China.

[#]Authors contributed equally to this work.

*Authors for correspondence:

Jun Li, Ph.D. Tel: +86 028 82890981

Email: lijun@cib.ac.cn

Yu Zhao, Ph.D. Tel: +86 028 85422436

Email: yuzhao@wchscu.edu.cn

Hua-Jun Wu, Ph.D. Tel: +86 010 82805976

Email: hjwu@pku.edu.cn

Abstract:

Disruption of cochlear architecture and development can lead to malfunction, resulting in hearing defects. However, the spatial molecular profiles critical for hearing function remain poorly understood due to the structural complexity of the cochlea. In this study, we performed comprehensive spatiotemporal transcriptomic analyses on the developing and adult cochlea, identifying numerous genes with gradient expression patterns in hair cells (HCs) and spiral ganglion neurons (SGNs) across the apical-to-basal axis. The gradient gene *Myo7a*, a well-known HC marker, established a decreasing gradient in outer hair cells (OHCs) from the apical to basal regions in adulthood. In contrast, the other class of gradient genes exhibited an opposing expression pattern to *Myo7a* along the cochlear axis in adulthood, such as *Calb2* in HCs and *Nefh* in SGNs, which potentially corresponds to the cochlear tuning properties for sensing gradient frequency sounds. Importantly, our analyses provided compelling evidences for the existence of distinct spatial subtypes of OHCs. The spatial analyses revealed regional heterogeneity in cell communication intensity between HCs and SGNs, with the weakest intensity at the apex, potentially aligning this region for detection of low-frequency sound. This study systematically characterized the fine spatial organizations in HCs, SGNs, and their regionalized cell-communications within the cochlea, offering insights into the morphological and molecular foundations underlying cochlear tonotopic organization and frequency discrimination.

Keywords: spatiotemporal transcriptomics, spiral ganglion neuron, outer hair cell subtypes, gene expression gradients, cochlear development, tonotopic organization

Introduction

The inner ear is one of the most structurally and functionally complex organs in vertebrates, comprising the cochlea and vestibular apparatus [1]. The cochlea is responsible for converting sound waves into neural signals, while the vestibular system aids in maintaining equilibrium [2, 3]. Development of inner ear is a highly coordinated process involving gene expression regulation, cellular differentiation, morphogenesis, and the activation of signaling pathways [3, 4]. The intricate architecture of inner ear is crucial for its sensory functions, and most genetic variations affecting its structure will cause sensory impairments. Cochlear and vestibular dysfunctions can result in significant auditory and balance disorders, such as congenital hearing loss, age-related hearing degeneration, and vestibular disorders, which underscores the need for deeper insights into inner ear development and function [3, 5]. Sensorineural hearing loss (SNHL) is one of the most prevalent chronic diseases, often caused by aging and noise overexposure. SNHL typically affects high-frequency regions, though low and mid-frequency regions may also be involved depending on the etiology [6-8]. The cochlea exhibits a tonotopic gradient to sound frequencies along its longitudinal axis, from the base to the apex [9]. Hair cell (HC) loss or spiral ganglion neuron (SGN) damages are more predominant in the basal region under stresses, ototoxic drug exposure, or during aging [10-12]. Despite significant research, the molecular and cellular mechanisms underlying tonotopic organization and frequency-specific damage remain incompletely understood, in part due to the complexity and inaccessibility of this deeply embedded organ [10, 13-15].

Recent advances in single-cell transcriptomics have revolutionized our understanding of inner ear biology, encompassing developmental processes [13, 16-18], age-related hearing loss (ARHL) [19], noise-induced hearing loss [20], ototoxic hair cell death [21], and hair cell regeneration [22]. This technology provides high-resolution insights into cell population heterogeneity within the inner ear, enabling the identification of novel cell types and constructions of developmental trajectories that were usually neglected in traditional bulk RNA sequencing approaches. For example, single-cell transcriptomics has facilitated the identification of rare cell types or transitional cell states involved in hair cell regeneration [22, 23], as well as new subtypes of SGNs in the cochlea [24-26]. These insights are invaluable for elucidating cellular contributions to inner ear structure and function, and for identifying potential therapeutic targets.

However, single-cell transcriptomics has certain limitations [27], notably the loss of spatial context, which is essential for understanding inner ear function. The spatial organization of cells is often disrupted during tissue dissociation, obscuring key insights into cell localization and interactions within the broader tissue structure [28]. For instance, single-cell transcriptomic studies have uncovered different SGNs subtypes [24, 26], however, their spatial distribution along the tonotopic axis remains unclear. Recent immunostaining studies have shown that type I SGN exhibited differential distribution across cochlear regions [10], but the molecular mechanisms governing this phenomena remain elusive, partly due to the loss of spatial information in single-cell RNA sequencing (scRNA-seq) data.

Spatial transcriptomics has emerged as a transformative approach, maintaining the spatial organization of cells while providing transcriptomic data [27]. Recent advances have enabled researchers to explore the spatial and temporal dynamics of gene expression in complex tissues like the heart [29, 30] and brain [31]. In the context of the inner ear, spatial transcriptomics allows for precise localization of gene expression, facilitating the study of tonotopic organization, development, and pathology. It also enables the integration of transcriptomic data with morphological findings, helping validate cellular identities in relation to specific tissue structures [28, 30]. Additionally, spatial transcriptomics offers insights into microenvironments and cell-cell interactions that drive organ development and function [32].

In this study, we aimed to establish the single-cell resolution spatial transcriptomic profile, and decipher the molecular basis of intricate architecture of cochlea, especially its tonotopic organization. By integrating spatial, single-cell transcriptomics, and RNA *in situ* validations, we found that a number of hair cell marker genes like *Myo7a* and neuronal marker genes like *Nefh* appeared in a gradient expression pattern along the cochlear axis, revealed that HC and SGN subtypes exhibit finely tuned spatial arrangements. Furthermore, spatial differential gene expression analyses revealed regional heterogeneity of cell communication intensity between HCs and SGNs, with the weakest in the apex, potentially aligning this region for detection of low-frequency sound. These gradient patterns of critical marker genes, the regionalized heterogeneity of HCs or SGN subtypes, and spatially divergent cell communications are mirrored with the tonotopic organization along the cochlear axis. Many of these gradient genes

are associated with deafness or hearing defect, suggesting that disruption of their functions or gradient pattern may result in hearing defects. These findings offer valuable insights into the molecular mechanisms underlying the tonotopic organization of auditory sensitivity along the cochlear axis.

Results

Spatiotemporal characterization of cochlear cell types at different stages

To elucidate the molecular mechanisms of cochlear morphogenesis and its functional establishment during development, we conducted spatial transcriptomic analyses of the cochlea across three different important stages, including embryonic stage 17.5 (E17.5), postnatal stage 8 (P8), and adult stage (2M), respectively (Fig. 1a). During development, the structures of the inner ear undergo dynamic changes, ultimately forming a complex and highly specialized architecture in adult stage (Fig. 1b). Notably, the cochlea is a spiral structure rich in chambers, formed by various cell types that are intricately and spatially organized in an ordered manner (Fig. 1b) [1]. The spatiotemporal single-cell atlases were first established, and 5,545, 10,214 and 7,414 spots were obtained from single E17.5, P8 and 2M mouse cochlea section samples at a resolution of 10 μm, respectively.

In general, the spatial transcriptomic data have lower resolution and relatively low quality of cell clustering, compared to routine scRNA-seq data [27]. Integration of scRNA-seq and spatial RNA-seq will facilitate the spatial data analyses and enhance the powers of each other. Therefore, the E17.5 and P8 cochlear scRNA-seq data from previous publications [17], and the single-nucleus RNA-seq (snRNA-seq) data of the

adult cochlear from our previous publication [33] were re-analyzed and compared with the spatial transcriptomic data. The gene markers from previous scRNA-seq studies [17, 24, 26, 33] were used for spatial clustering and cell type identification. Totally, 22 cell types were annotated in E17.5 cochlea (Fig. S1a), 28 cell types in P8 cochlea (Fig. 1b), and 21 cell types in 2M cochlea (Fig. S1c), respectively.

According to the spatial distribution, all cell types from each dataset were briefly split into 8 groups including surrounding structure, fibrocyte, neuron, Schwann cell, Reissner's membrane, stria, root cell/spindle cell, and organ of Corti (OC) (Fig. 1d) (Table S1). Neither root cell nor spindle cell was identified in the dataset of E17.5 cochlea, but they were clearly identified in P8 and adult cochlea single-cell atlases with markers *Aqp5* and *Slc26a4*, suggesting these cells were differentiated cell type in postnatal stage (Fig. 1c, d, and S1). The surrounding structure mainly contained outer structure, identified with *Col1a1* and *Mmp9* gene markers, Neutrophils with by *Retnlg* and *Lcn2* gene markers, chondrocyte and pericytes with *Mgp*, *Slc38a2* and *Gja4* gene markers, and Osteoblast with *Panx3* and *Satb2* gene markers (Fig. 1c). Fibrocytes of cochlea mainly distributed in the spiral ligament (SLg) and limbus (SLb) [34], and both were discovered in each dataset. Four subtypes of SLg fibrocyte were identified by *Car3* and *Otor* in P8 dataset.

The neurosensory epithelium of cochlea plays a crucial role in auditory sensory, which mainly comprises OC and SGN. The neuron cells were found mainly existed in the three regions near the cochlea duct with the known neuron markers (*Nefh*, *Snap25*, *Nefl* and *Meg3*) (Fig. 1c, S1b and c) [35-37]. Distinct cell types identified in the OC

revealed the high cellular heterogeneity during hearing establishment and maturation, such as 7, 10 and 6 cell types in E17.5, P8 and adult samples, respectively. In the OC of P8, interdental cell with gene markers *Otoa* and *Rspo2*, inner sulcus cell with gene markers *Aqp4*, inner phalangeal cell/inner border cell with gene markers *Far1* and *Tecta*, Hensen's cell and outer sulcus cell with gene markers *Frzb* and *Umodl1*, outer hair cell (OHC) and inner hair cell (IHC) with gene markers *Otof*, and Deiter cell/pillar cell with gene markers *Lgr6* were observed (Fig. 1d).

Spatial organization of cochlear lateral wall cell types

After brief identification of cochlear cell types, several specific cochlear structures and cell types were further spatially analyzed in details to validate the spatial single cell atlas. The lateral wall, balancing the endocochlear potential, was composed of stria vascularis and spiral ligament, which is one of the important parts of the scala media (Fig. 2a) [34]. There were three cell types in the location of stria vascularis from E17.5 and P8 samples, including basal cells, intermediate cells and marginal cells that identified by *Dnase1*, *Hpse* and *Dct*, respectively (Fig. 2 and S2). The results revealed a strong correspondence between the spatial data and the single-cell level RNA-seq data (Fig. 2c, S2b and c), according to the marker genes for each lateral wall cell types [17, 33]. But only basal cells and marginal cells were annotated in the adult dataset, using *Dct* and *Kcne1* markers (Fig. S1c, d). The intermediate cells were not identified, probably due to ossified structures in adult cochlea which hinders the tissue sections and detection of mRNA.

RNA *in situ* assays targeting these above markers were performed to confirm the

cell type annotation. *Dnase1* and *Enpep* are expressed in the stria vascularis specifically (Fig. 2d, e), which is consistent with their expression profiles revealed by spatial data analyses. Next, root cell/spindle cell were identified between outer sulcus cell and stria vascularis with specific high expression of *Aqp5* and *Kcne4* (Fig. 2b, c), which was consistent with our previous cochlear snRNA-seq study [33]. In addition, four types of fibrocytes were identified in the lateral wall, based on spatial location and known markers (Car3, Otor and Otos) (Fig. S1d, S2, Table S1) [20]. The spatial expression analyses of lateral wall cell types, in combination of snRNA-seq data and RNA *in situ* validation, revealed the accuracy and resolution of our spatial single-cell atlas.

Temporal expression pattern changes of spiral ganglion neurons

The spatial data analyses further identified SGNs, which are the primary neurons responsible for conveying sound signals from HCs (Fig. 3a, above), in the exact regions where SGNs are supposed to locate (Fig. 3a). Type I and type II are two main subtypes, constituting of 90-95% and 5%-10% in the SGNs, respectively. Type I SGNs were further divided into subtype Ia, Ib, and Ic [35, 37]. An additional subtype, type III was discovered in our recent study (Fig. 3b) [33]. Due to close similarity of each SGN subtype, it is challenging to further identify each SGN subtype from these spatial sequencing data. Therefore, RNA *in situ* detections with several SGN markers were performed to identify SGN subtypes. *Meg3* was highly expressed in neuronal type I at all three sites of cochlea (apical, middle, and basal) (Fig. S3-1a), consistent with its painting profile in cochlear spatial sections. Slightly stronger expression of *Meg3* were observed in the basal region than the apical region (Fig. S3-1a). In addition, the RNA

in situ result of *Cend1*, which is mainly expressing in type I and III SGNs, also showed the similar expression pattern as *Meg3* (Fig. S3-1b). The type II SGN marker genes *Cilp* and *Flt3* exhibited relative stronger expression levels in the apical SGNs (Fig. 3b, S3-1c, d).

Schwann cells, the supporting cells of SGNs, were also identified and classified into three subtypes displaying unique gene expression profiles (Fig. S3-2b, Fig. S3-2c, e). Type I Schwann cells were characterized by elevated expression levels of *Prx*, *Plp1*, and *Pllp* (Fig. S3-2c, f), suggesting their role in myelination processes [38]. Type II Schwann cells showed high expression of *Clu* and *Fabp7* (Fig. S3-2c), indicating a potential involvement in lipid metabolism and cellular stress responses [39]. Meanwhile, type III Schwann cells had distinct expression patterns with genes like *Smpd3*, *Htra1*, and *Ly6e* (Fig. S3-2c). These expression profiles underscored the functional diversity within Schwann cell populations and their supporting neural function in the inner ear. The accuracy of our spatial transcriptome data that was validated by our previous snRNA-seq data and RNA *in situ* assay (Fig. S3-2d). In total, the data demonstrated a good consistency of spatial data with snRNA-seq and RNA *in situ* results, revealing the quality of our spatial single-cell atlas.

To explore the molecular changes that occur within the neuronal differentiation and maturation, we fitted a principal tree in diffusion space to show the temporal dynamics of SGN development. The tree was represented into a dendrogram recapitulating a branched trajectory based on the transcriptional similarity of pseudotime-ordered cells (Fig. 3c and S3-1c). We further used differential gene expression (DEG) approaches

that characterize pseudotime-ordered molecular trajectories. Focusing on genes with significant variations (Fig. 3c and S3-1d), we observed that the shared, unspecialized neurons' trajectory was characterized by rapid downregulation of genes *Rpl4* and *Tubb2b* commonly associated with early neuronal differentiation processes, and upregulated of genes *Snap25* and *Spp1* that are involved in specification events in cochlea and other systems. The bubble diagram more visually illustrated the dynamics of these genes during development (Fig. S3-1d). The differential marker gene expression analyses revealed the relatively higher expression of *Snap25*, *Spp1* and *Atp1b1* in adult neurons, while genes such as *Calb2*, *Rps7*, *Eef1a1* and *Tubb2b* showed relatively higher expression at earlier stages (Fig. 3c and S3-1d). This spatiotemporal dynamic gene expression pattern of SGN was further validated by immunostaining with Calb2, which was dominantly expressed in type III and type Ia SGN subtypes (Fig. 3b and d) [10]. At E17.5 stage, the highest expression level of Calb2 was detected at the apical region, medium at the middle region, and weak at the basal region (Fig. 3d, left). This pattern was gradually changed at P8 stage (Fig. 3d, middle), and finally reversed in the adulthood, with the highest expression level of Calb2 in the basal SGNs (Fig. 3d, right). These spatiotemporal dynamics of gene expressions reflected the molecular mechanism of development and maturation of SGNs from E17.5 to adulthood.

Gradient expression of neuronal marker genes across the apical-to-basal axis

To investigate the spatial differences of SGNs, we performed local single-cell analyses from apical to basal regions of cochlea. Neuron cells from three distinct regions (apical, middle, and basal) were isolated according to cell identifications and

their spatial coordinates from the total spatial single cell atlas (Fig. 4a and S4a, d). After pairwise comparisons among apical, middle, and basal SGNs, the obtained differentially expression genes (DEGs) were intersected with the neuron-specific gene list from snRNA-seq dataset and spatial dataset (Table S1). Finally, 323, 470 and 1587 genes were identified from E17.5, P8, and adult datasets, respectively (Table S2).

For E17.5 spatial dataset, the SGNs from apical, middle, and basal regions were extracted (Fig. S4a). *Nefm*, *Nefl*, *Trim2*, and *Sema3e* genes were highly expressed at the apical region and relatively lower in the basal region (Fig. S4b, c). *Nsg1* and *Cd200* genes showed opposite expression pattern (Fig. S4b, c). Two obvious contrary expression patterns were maintained at P8 stage (Fig. 4b, c). Genes like *Nefh*, *Cend1*, and *Calb2* were expressed higher at basal region, but *Sema3e*, *Rian*, *Myo16*, and *Cdh9* were expressed higher at the apical region (Fig. 4b, c). RNA *in situ* and immunostaining with these gradient markers *Nefh* and Calb2 were performed to validate the gradient expression pattern. *Nefh* mRNAs are most abundantly detected at the basal region, less at the middle, and very weak at the apical region (Fig. 4d-g). Calb2 antibody immunostaining also displayed similar pattern, but the variation of gradient was not as sharp as *Nefh* (Fig. 4d-g) at P8 stage. Note that both *Nefh* and Calb2 expression patterns were reversed between E17.5 and P8 stage (Fig. 3, 4, S4). Interestingly, *Nefh* expression gradient was reversed again in adulthood (Fig. S4d-f). Furthermore, according to SGN markers from the published data [24, 26, 33], three subtypes of neurons were annotated in the three regions respectively (Fig. 4e-g). *Nefh* was commonly expressed in all SGN subtypes but with higher expression level in subtype III [33]. The relative higher

expression of *Nefh* in basal region suggested that SGN subtype III may be predominantly located at the basal region. The expression of other gene markers suggested that SGN subtypes may exhibit a similar gradient distribution along the cochlear axis basing on their marker gene expressions (Fig. S3). These spatiotemporal dynamics of neuronal gene expression gradients and distributions of SGN subtypes revealed the progress of SGN development and differentiation along the cochlear axis.

Spatiotemporal profiling of the organ of Corti development

The OC is embedded in the cochlear duct and rests on the basilar membrane (Fig. 5a), allowing it to be finely tuned to different frequencies of sound [40]. UMAP visualization demonstrated distinct OC cell types, including inner and outer hair cells (IHCs and OHCs), Deiter cells, pillar cells, Hensen's cells, tympanic border cells and inner sulcus cells (Fig. 5a, b). A UMAP plot from our previous single-nucleus transcriptomic (snRNA-seq) dataset [33] illustrated the clustering of different cell types in the inner ear based on gene expression profiles (Fig. S5a). The expression profiling of key marker genes across various identified cell clusters in the snRNA-seq dataset (Fig. S5b, c), consistent with the spatial transcriptomics findings (Fig. 5c, S5d), reinforcing the identification of these cell types. For example, *Otoa* was predominantly expressed in interdental cells, while *Ocm* was highly expressed in the OHCs (Fig. 5c). Overall, the consistent patterns observed between spatial transcriptomics and scRNA-seq data confirmed the accuracy of cell type identification and their respective marker genes, providing a comprehensive view of cochlear cell diversity.

To further understand the changes of expression pattern occurring in the process of

hair cell maturing, we fitted a master tree for hair cells from three stages in diffusion space. The tree was then represented as a dendrogram that reproduced a branching trajectory based on the transcriptional similarity of the proposed time-ordered cells (Fig. S5e). The generated tree accurately reflected the developmental stage branching characteristics. Dynamic gene expression changes across the three stages were demonstrated by heatmaps, with genes such as *Ocm* and *Nnat*, displaying distinct temporal expression patterns (Fig. S5f). The expression of genes such as *Ocm*, *Otos*, and *Tectb* showed dynamic changes from E17.5 to adulthood, further validating transcriptional changes in cochlear development (Fig. S5h). The proposed temporal trajectories of key genes were demonstrated, illustrating the dynamics of cellular expression during developmental stages (Fig. S5g). The expressions of *Apod*, *Otof*, *Nnat*, and *Tectb* are peaked in expression during different developmental windows, reflecting their roles in hair cell maturation. Overall, this analysis revealed the key spatiotemporal gene expression features within the OC that accompany the maturation of cochlear cell types and supporting structures critical for hearing function.

Spatiotemporal patterning of cochlear hair cells reveals the existence of outer hair cell subtypes

The hair cells (HCs) were defined around E16.5 stage following a basal-to-apical gradient [41]. All the HCs were well differentiated at E17.5, including the apical regions with relative weaker expressed marker Myo7a (Fig. 5d). No significant differences of Myo7a signals were observed between IHCs and OHCs from apex-to-base. At P7 stage, the Myo7a expression in apical region was clear and became stronger

compared to E17.5 cochlea, revealing further differentiation of hair cells in the apex. The expression of Myo7a in the middle region was relatively stronger than that in the apical and basal regions (Fig. 5e). In adulthood, the Myo7a expressions of IHCs display an averaged pattern from apex-to-base, relatively slightly higher in the middle region (Fig. 5f). While the Myo7a expression in OHCs showed a huge divergence from apex-to-base (Fig. 5f, g). The basal OHCs expressed very low level of Myo7a (Fig. 5g). It's worth noting that the sharp contrast of Myo7a signals between IHCs and OHCs in the basal region (Fig. 5g). At the middle region, the expression Myo7a was gradually increased in OHCs following a basal-to-apical gradient (Fig. 5g). The Myo7a signals of OHCs and IHCs showed less divergence along the gradient and became no obvious divergence at the apex (Fig. 5f, g).

To further validate this expression gradient in OHCs, a large number of spatial differentially expressed genes (DEGs) were isolated from E17.5 (Fig. 6a, S6-1a-d, Table S3), P8 (Fig. S6-1d, Table S3), and adulthood (Fig. 6b, Table S3). After filtering and intersecting with a dataset of HC-specific genes (Table S1), 184, 265, and 205 DEGs were retained for the three datasets, respectively. There are two patterns of gene expression gradients for these spatial DEGs. In adulthood, genes like *Myo7a*, *Asb1*, and *Cachd1* displayed a decrease gradient from apical to basal pattern, whereas genes *Fat2*, *Fam83f*, and *Cab39* showed a reversed gradient (Fig. 6b). These spatial DEG data, particularly the *Myo7a* gene, were well matched with Myo7a immunostaining results in the whole amount (Fig. 5f, g) and sections (Fig. 6c) of adult cochlea. The OHCs at the apical regions showed comparable Myo7a signal intensity with IHC, while the

Myo7a expression was relatively lower than the IHCs in the basal region (Fig. 5f, g and 6c). But this Myo7a gradient was developmentally dynamic at the E17.5 and P8 stages (Fig. S6-1d-f) and only established in adulthood. The immunostaining results were consistent with the spatial differential expression results (Fig. S6-1d-f), revealing the value of these spatial data and the accuracy of data analyses. Importantly, the spatial DEG analyses and the validation by immunostaining both provided compelling evidences that the adult OHCs from apex to base are spatially distinct subtypes, as revealed by their different or even reversed gradient patterns of HC marker gene expressions.

Spatiotemporal dynamics of communication between hair cells and SGNs reveal the tonotopic organization along cochlear axis

To understand how HCs cooperate with SGNs to sense and convey different-frequency sound signals, we interrogated secreted signaling events among cochlear epithelium and SGN for the three spatial datasets. At E17.5 stage, the maximum number of interactions is found between SGNs and HCs, when the SGNs were the hub (Fig. S7-1a, b). This result was consistent with core function of SGNs for receiving the signals from HCs. Whereas, the stronger communications are observed between supporting cell subtypes and HCs when the HCs were the hubs (Fig. S7-1b, right). These results revealed that HCs are the center of cell connections in cochlea, communicating with nearby supporting cell types to coordinate its sensory function, not only just connecting with SGNs. At P8 stage, the number of interactions increased, either between SGNs and HCs or other cell types (Fig. 7a, b). As for HCs, the strength

of interaction with neighbor cells like inner sulcus cell and interdental cell (lateral Kolliker's organ), as well as Hensen's cell became stronger (Fig. 7b, S7-1b).

Next, all pathways were analyzed and ranked according to their communication intensity. The interaction strength of Ptn-Sdc, Mdk-sdc, and Fgf pathways were among the top 3 of all the interactions (Fig. S7-2). Fgf signaling pathway plays crucial roles in inner ear development and were further analyzed between these cell types of OC [42]. When neurons acted as the signaling source, it interacted with cells from the OC mainly by Fgf10-Fgfr2 signaling both at E17.5 and P8 stages (Fig. 7c, S7-1c). When HCs acted as the signaling source at P8, it mainly interacted with other cells from the OC by Fgf8-Fgfr2 signaling, especially with Deiter cell/pillar cell (Fig. 7c). While HCs mainly interacted with other cells by Fgf10-Fgfr1 (Fig. 7c). With RNAscope assay, the expression location of *Fgf10* and *Fgfr2* were confirmed, which was largely consistent with spatial expression result (Fig. 7e, f). Strong expressions of *Fgf10* and *Fgfr2* were detected in OC and SGN regions. Interestingly, their expressions both exhibited a obvious gradient in SGNs, decreasing from apical to basal regions, suggesting spatial differences of cell communications across the cochlear axis.

Next, regionalized cell communications were further analyzed across the cochlear axis. The OC cell types from apical, middle, and basal regions were extracted from the whole spatial single-cell atlas, and were subjected to differential cell communication studies. The overall cell communications were weak at the apical region, but relatively stronger in the middle and basal regions (Fig. 8a-c). The strongest communications are found in the middle region (Fig. 8b), which may serve as the hub regions in the cochlea.

These regionalized heterogeneities of the connection intensity between SGNs and HCs (Fig. 8a-c) were confirmed by the immunostaining assay with Tuj1 (also known as βIII-tubulin), which is a widely recognized marker for neuronal cells [43] and is often used for detecting the neuronal projections of SGNs in the inner ear [44, 45]. The immunostaining of Tuj1 revealed the strongest signal intensity of Tuj1 in the middle region rather than the apical and basal regions (Fig. 8d, e), suggesting their strong connections in the middle region. These projection features of SGNs revealed by immunostaining (Fig. 8a-c) was consistent with the differential communication studies in three different regions (Fig. 8d, e).

In this study, the spatiotemporal transcriptomic analyses revealed the developmental dynamics of HCs and SGNs and demonstrated their gradient gene expression patterns from apex-to-base, and their regionalized communications as well. These spatiotemporal data provided deeper insights into the molecular and cellular mechanism underlying the tonotopic organization along cochlear axis. According to these results, a model was proposed to illustrate the underlying mechanism for tonotopic organization (Fig. 8f). The cochlea organized its cell types in a spatially specific manner. The HCs and SGNs expressed a number of genes, like *Myo7a*/*Ocm* in HCs and *Calb2*/*Nefh* in SGNs, in a gradient pattern from apex to basal, either in a decreased or increased manner (Fig. 8f). Accordingly, their communications are toned into a spatially regionalized pattern with divergent connection intensity from apical to basal regions. These variant gradients patterns are mirrored by gradient features of sound frequency sensitivity along cochlear axis, which may be the molecular

fundamentals for establishing the tonotopic organization.

Discussion

In this study, we performed spatial transcriptomic sequencing of the inner ear at various developmental stages, creating a single-cell resolution atlas of the cochlea with detailed spatial gene expression profiles. This approach enhanced traditional tissue section RNAScope assays by enabling the examination of spatial expression profiles across different developmental stages and specific cell types. Due to the inherent limitations of the spatial technology itself, spatial transcriptomics still has some intrinsic issues that are difficult to resolve [27, 46]. The spatial stacking between cells is unavoidable and the thickness of cell bodies left in a tissue section is also spatially dynamic, which can all compromise the resolution and accuracy of differential expressing gene study. Despite less resolution compared to previous inner ear scRNA-seq or snRNA-seq datasets, the spatial single-cell atlas established in this study is valuable for single-cell level transcriptomic analyses. The spatial datasets served a valuable resource for researchers investigating inner ear development and auditory function, allowing for the exploration of spatiotemporal gene expression patterns of any gene of interest, or any particular region of interest.

Our analyses identified distinct spatial expression patterns of SGNs subtype marker genes, suggesting the spatial differentiation of SGN subtypes along the cochlear axis. Our previous work newly identified an additional SGN subtype, type III [33], which is very similar with type I SGNs according to their commonly expressed marker genes. Our results showed that the type III marker gene *Nefh* displayed a gradient

pattern with high expression level predominantly in basal regions (Fig. 4), suggesting that the type III SGNs dominantly located in basal region. A recent study using conventional immunostaining demonstrated differential distribution of SGN subtypes along the cochlear axis, with type Ia and Ib neurons are primarily in apical and middle regions, while type Ic is more concentrated in the base [10]. However, the gene markers used in their study for distinguishing each SGN subtypes are different from ours, which may make certain inconsistent conclusions. They used Calb2 to label type Ia SGNs, Calb1 to label type Ib SGNs, and double negative Calb1$^-$/Calb2$^-$ to label type Ic SGNs [10]; while *Calb2* is dominantly expressed in type III and Ia according to our snRNA-seq data (Fig. 3b). But the same conclusion is that the SGN subtypes exhibit a divergent distribution along apical-basal axis.

Interestingly, our results showed the gradient patterns of those marker genes for each SGN subtype is temporally dynamic, such as that the gradient expression of *Nefh* and *Calb2* in SGNs at embryonic stage is reversed in adulthood. These spatiotemporally dynamic patterns but similar molecular features among subtype Ia, Ib, Ic, and III suggest that each SGN subtype represent a cell state of type I SGNs across different cochlea regions or across different stages. Type III SGNs (Fig. 4), may represent a new subtype of type I SGNs [10]. The type III SGNs were not identified in previous studies likely due to different approaches (scRNA-seq or snRNA-seq) and different developmental stages (developmental or adult stages) used in these studies [13, 24, 26]. The loss of spatial information might be an additional reason. Traditional histological and immunostaining methods are limited in their ability to achieve comprehensive

large-scale molecular characterization and differential expression analysis of SGN subtypes [10]. The close molecular characteristics of type I and III SGNs complicate their distinguishing. Our spatial data indicate that these subtypes may represent the same cell type (type I) exhibiting subtle molecular differences based on their spatial location along the cochlear axis, contributing to tonotopic organization [10, 33].

In addition to SGNs, HCs also exhibit spatial gradient heterogeneity along the cochlear axis. Our findings reveal notable differences between OHCs located in the basal and apical regions, while IHCs exhibited less divergence across these regions. Classic markers like *Myo7a* show a pronounced gradient from apex to base, indicating distinct molecular identities. Other proteins, including Prestin (Fig. S6-2), *Calb2*, *Kcnq4* and BK channels, were also reported to display gradient distributions [9]. Despite some inconsistences due to limited hair cell numbers in our spatial dataset, many reported gradient genes were confirmed by our spatial data, confirming obvious spatial heterogeneity of OHCs. Currently, no single-cell transcriptomic studies have reported the subtypes of OHCs in mice due to very limited number of HCs captured. Our spatial data and immunostaining results provided clear evidences for the existence of distinct OHC subtypes. Moreover, these findings suggest that OHCs may be also spatially subdivided into distinct subtypes, similar to SGN subtypes.

Importantly, our analysis uncovered numerous genes exhibiting gradient expression patterns along the cochlear axis, indicating that these gradients may contribute to the regional specialization or patterning of frequency sensitivity in the cochlea. Many gradient genes identified from earlier developing cochlea in previous

publications are associated with the development [13]. These gradient expression patterns are transient, reversed, or disappeared in the later stages. In contrast, the gradient genes identified in this study from the adult stage are primarily associated with energy metabolism and neural activity (Fig. S4). This association highlights the ultimate forms of cochlear organization and their sensory functions. Therefore, the gradients from later stages, rather than those from earlier developmental stage, are more likely to align to the gradient patterning of frequency discrimination functions in the cochlea. Furthermore, our data revealed regionalized differences in cell-cell communication within the cochlea, emphasizing the importance of regionalization in the inner ear's functional organization. Understanding these localized interactions is crucial for uncovering the mechanisms governing cochlear development and its ability to perceive sound frequencies with high precision. Overall, this study highlights the temporal and regionalized gene expression patterns, along with the specialized organization and communication among cell types, including hair cells, SGNs, and supporting cells. This coordinated mechanism is essential for establishing tonotopic patterning during development and achieving precise sensory function.

Given the structural complexity of the inner ear, spatial organization is crucial for auditory function. Genetic variations affecting its morphology often result in hearing defect [47, 48]. While single-cell RNA-seq has been widely used in inner ear development research and has yielded a wealth of insights into inner ear development, it lacks the crucial spatial context essential for understanding developmental and genetic mechanisms. In contrast, our spatial transcriptomic analysis preserves this

spatial context, providing significant advantages for studying inner ear development and architecture. Our spatial transcriptomic analysis offers invaluable insights that address these challenges and will undoubtedly have significant implications for the field. We mapped the expression patterns of known deafness-associated genes on inner ear tissue, revealing spatial expression hotspots that identify structures most vulnerable to mutations causing hearing loss (Fig. S9). Many of gradient genes identified in this study are associated with deafness or hearing defects, such as *Myo7a*, *Calb2*, *Fgf10*, *Eya1*, and *Gata3*, whose mutation were reported to cause morphological abnormality of inner ear or hearing defects [49]. These spatial data offer important resources for the discovery of deafness-causing genes and investigation of the pathogenic mechanisms underlying hearing defects.

Methods

Animal and tissue collection

Wild-type C57BL/6 mice were bred in the laboratory. All animal experiments were conducted with approval from the Animal Research and Ethics Committee of the Chengdu Institute of Biology, Chinese Academy of Sciences (Approval No. CIBDWLL2018030). For E17.5 cochlear tissue, a pregnant female was euthanized and inner ears were dissected from pups. For postnatal time points, P8 and Adult mouse were euthanized and inner ears were dissected. Cochlea were separated from the inner ears under the stereo microscope (Olympus, SZ61) and washed by ice-cold DPBS. After wiping the liquid by dust-free paper, cochleae were rinsed with ice-cold OCT, and next moved into Cassettes with ice-cold OCT. In order to gain better longitudinal section

with at least 4 cochlea duct regions, the tissue position in the cassette was fine-tuned under the stereo microscope again. Then the cassettes were quickly put on the dry ice to ensure the tissues were froze immediately. All samples were sent to Beijing Biomarker Technologies Co. the same day.

Tissue cryosection and processing for spatial-seq

The spatial-seq was performed with the BMKMANU S1000 Gene Expression kit (BMKMANU, ST03002). Tissue sectioning, RNA quality, HE staining, imaging and tissue optimization were followed by the BMKMANU S1000 Tissue Optimization kits user guide (BMKMANU, ST03003). The Cryosections were cut at a thickness of 10 μm and every section would be checked with HE staining before target structure section appearing. When 4 cochlea duct holes were observed, the next section would be moved to slide for later sequencing.

Library preparation and sequencing

Library constructions were also performed according to the BMKMANU S1000 Library Construction Kit User Guide. The Illumina library was sequenced with Illumina NavoSeq 6000. The raw data from Illumina and Nanopore were mapped to the mouse reference genome (GRCm38, ftp://ftp.ensembl.org/pub/release-74/fasta/mus_musculus/) by BSTMatrix v2.4 (http://www.bmkmanu.com/wp-content/uploads/2024/07/BSTMatrix_v2.4.f.1.zip) and BSTMatrix-ONT v1.2 (http://www.bmkmanu.com/wp-content/uploads/2023/03/BSTMatrix-ONT_v1.2.zip), respectively, using default parameters. The image adjusted by BSTViewer V4.7 (http://www.bmkmanu.com/wp-content/uploads/2024/07/BSTViewer-V4.7.4.1.rar)

and corresponding level 2 (10 μm) matrix were used for downstream analysis.

Cell clustering and cell-type identification

Downstream analysis of BSTViewer output data was performed using the R package Seurat (v5.1.0) (https://github.com/satijalab/seurat) [50]. HE images from the same sample were pooled together as a data set for analysis. First, for all samples, data was preliminary filtered with min.cell at 5 and min.fearture at 100, when imported into R. Then all datasets were normalized (scale.factor=10000) and scaled using all genes. Principal component analysis (PCA) focusing on the most variable features was performed and for all data, the first 30 dimensions obtained by RunPCA were applied to the analysis of RunUMAP, FindNeighbors, and FindClusters to obtain UMAP and cluster information. Cluster specific genes were identified by FindAllMarkers differential expression analysis. Combining cell-type specific markers identified by Seurat and previously reported markers, spot' ident was annotated.

Cell communication analysis of hair cells and supporting cells

Cellchat (v1.6.1)[51] package was applied to explore the potential interaction pattern of cell types from OC and SGN. Based on the normalized gene-expression matrix of our datasets, the database of mouse ligand-receptor interactions was used to identify overexpressed genes and interactions with the method of "trimean", compute the communications and related pathways. All analysis steps were followed by the suggested workflow of CellChat with the default parameters.

Pseudotime trajectory analysis of HC and SGN groups

The newCellDataSet function of Monocle2 (2.32.0) [52] was utilized to create a

CellDataSet object, and the estimateSizeFactors and estimateDispersions functions were applied for the estimation of size factors and dispersions, respectively. By employing the detectGenes function, genes expressed in at least 10 cells were identified, and key genes for trajectory inference were set using the setOrderingFilter function. Subsequently, the reduceDimension and orderCells functions were applied for dimensionality reduction and cell ordering to construct the pseudotime trajectory of cells. The plot_cell_trajectory function was used to visualize the cellular trajectories, which were colored according to cell states. Additionally, genes with expression changes during cell development and genes that regulate the branching points of cellular differentiation were identified using the differentialGeneTest and BEAM functions. Finally, a heatmap of pseudotime-associated genes was generated using the plot_pseudotime_heatmap function to display the expression patterns of these genes across different cellular states.

Gene expression pattern analysis from apex to basal part

To explore regional gene-expression characteristics along the cochlea duct, the expression matrixes of SGN and organ of Corti cell types from apex, middle-basal and basal reagions (Fig. 4a; Fig S4a and d) were extracted separately for DEG analysis, with the method of wilcoxon test. To better reveal the expression pattern of differential genes, plot_density method from Nebulosa (V1.14) package[53] was used to depict spatial expression.

Immunofluorescence

Cochleae from E17.5, P8 and Adult mice were fixed in 4% paraformaldehyde

diluted in 1×PBS for 2 hours at 4 ℃, washed in 1×PBS for three times, dehydrated by 30% sucrose solution, then embedded in OCT Compound for cryosectioning at 10 μm thickness. According to previous publications [54], the immunofluorescence was performed as following steps. Briefly, sections were blocked in 5% bovine serum albumin (BSA, Biofroxx, 1110GR500)/10% horse serum albumin (HSA, Sangon Biotech, E510006-0100) / 0.5% Triton-X/1×PBS for 8~10 hours at 4 ℃ and primary antibodies were applied overnight at 4 ℃ in 5% BSA/10% HSA/0.5% Triton-X/1×PBS. All antibodies used were list in Table S1. Secondary antibodies were applied in 5% BSA/10% HSA/0.5% Triton-X/1×PBS for 6~8 hours at 4 ℃ followed by DAPI nuclear staining. All washes following primary and secondary antibody application were performed with 1% Triton-X/1×PBS. All fluorescent images were acquired using fluorescent microscope system (Nikon, Eclipse 55i). All antibody used in this study were listed in Table S4.

RNA *in situ* hybridization

The fragments of target genes (Table S4) were prepared by PCR amplification of cDNA from cochleae RNA, with reverse primers containing a T7 RNA polymerase promoter sequence. Next the DIG-labeled RNA probes were synthesized by the transcription reaction using Riboprobe Systerm-T7 kit (Promega, P1440) and DIG labeled UTP (Roche, 11277073910). The slides for RNA *in situ* hybridization (RNA-ISH) were prepared with the same steps of immunofluorescence. Then RNA-ISH was conducted as following steps, according to previous publications [33, 55]. Firstly, slides were fixed by 4% PFA for 5 min at RT and washed in 1×PBS for 3 min and in distilled

water for 1 min. Next for permeabilizing, slides were immersed in 0.2 M HCl for 15 min and 0.1 M triethanolamine-HCl for 10 min. After being washed in 1×PBS for 5 min, slides were dehydrated by washing for 20 min per wash in 75%, 85% and 100% ethanol. And then slides were treated by hybridization buffer containing DIG-labeled RNA probes overnight at 65 ℃. To remove non-specific and repetitive RNA hybridization, slides were washed in 5×saline sodium citrate (SSC) for 5 min at RT and 2×SSC for 30 min at 60 ℃. After being treated in 0.3% H_2O_2 for 1 h at RT, slides were blocked for 2 h at RT and next incubated with anti-DIG antibody overnight at 4 ℃. Finally, the signal was detected by the TSA® Plus Cyanine 3.5 (Cy3.5) detection kit (NEL763001KT, Akoya) and slides were sealed by diluted DAPI with glycerin. The images were captured by fluorescent microscope.

Statistical analysis

All statistical analyses were conducted by R and RStudio. And as for the results of wilcoxon-test, which were used to uncover the spatial differential expression genes for neuron cell and OHC, P-value < 0.05 were considered statistically significant.

Conflicts of interest

The authors declared no competing interests.

Data availability

The raw sequence data generated in this paper have been deposited in the Genome

Sequence Archive [56] in National Genomics Data Center [57], China National Center for Bioinformation, Beijing Institute of Genomics, Chinese Academy of Sciences (GSA: CRA019653) that are publicly accessible at https://ngdc.cncb.ac.cn/gsa. The ChIP-seq data of mouse inner ear from The mouse inner ear single-cell RNA-seq data at adult stage from our publication [33] have been deposited and can be accessible in the National Genomics Data Center under the number (CRA015540). The E17.5 and P8 single-cell RNA-seq data used for integration study were accessed under the number GSE137299 from previous publications [17, 18].

Acknowledgments

The work was supported by the National Natural Science Foundation of China (Nos. 82300142, 82301316, 32370882, and 32370536), and the Central Government Guides Local Science and Technology Development Funds in Sichuan Provincial (2022ZYD0131), and the Fundamental Research Funds for the Central Universities (BMU2021YJ064). We gratefully acknowledge the High-performance Computing Platform of Peking University for conducting the bioinformatics analysis.

Author's contribution

J. Li, Y. Zhao, and H. Wu designed the work; M. Yan, P. Zhang, H. Wang, J.H. Li, Y. Wang, X. Zeng, and Y. Gao acquired the data; M. Yan, H. Wang, Y. Wang, B. Zhu, D. Deng, F. Deng, X. Guo, L. Ma and Y. Feng analyzed the data; M. Yan, Y. Wang, and H. Wang made the figures; J. Li, Y. Zhao, and H. Wu wrote the paper.

References

1. Groves, A.K. and D.M. Fekete, *Shaping sound in space: the regulation of inner ear patterning.* Development, 2012. **139**(2): p. 245-257.
2. Torres, M. and F. Giráldez, *The development of the vertebrate inner ear.* Mechanisms of development, 1998. **71**(1-2): p. 5-21.
3. Wu, D.K. and M.W. Kelley, *Molecular mechanisms of inner ear development.* Cold Spring Harbor perspectives in biology, 2012. **4**(8): p. a008409.
4. Whitfield, T.T., *Development of the inner ear.* Curr Opin Genet Dev, 2015. **32**: p. 112-8.
5. Roccio, M., P. Senn, and S. Heller, *Novel insights into inner ear development and regeneration for targeted hearing loss therapies.* Hearing research, 2020. **397**: p. 107859.
6. Toppila, E., et al., *Individual risk factors in the development of noise-induced hearing loss.* Noise and Health, 2000. **2**(8): p. 59-70.
7. Kujawa, S.G. and M.C. Liberman, *Translating animal models to human therapeutics in noise-induced and age-related hearing loss.* Hearing research, 2019. **377**: p. 44-52.
8. Meghji, S. and J. Phillips, *The significance of audiometric notching in individuals with a history of noise exposure: a systematic review.* Ear and Hearing, 2021. **42**(5): p. 1109-1118.
9. Mann, Z.F. and M.W. Kelley, *Development of tonotopy in the auditory periphery.* Hearing research, 2011. **276**(1-2): p. 2-15.
10. Wang, M., S. Lin, and R. Xie, *Apical-basal distribution of different subtypes of spiral ganglion neurons in the cochlea and the changes during aging.* Plos one, 2023. **18**(10): p. e0292676.
11. Atkinson, P.J., et al., *Sensory hair cell development and regeneration: similarities and differences.* Development (Cambridge, England), 2015. **142**(9): p. 1561.
12. Ding, D., H. Jiang, and R.J. Salvi, *Mechanisms of rapid sensory hair-cell death following co-administration of gentamicin and ethacrynic acid.* Hearing research, 2010. **259**(1-2): p. 16-23.
13. Wang, S., et al., *3D reconstruction of the mouse cochlea from scRNA-seq data suggests morphogen-based principles in apex-to-base specification.* Dev Cell, 2024. **59**(12): p. 1538-1552 e6.
14. Tobin, M., et al., *Stiffness and tension gradients of the hair cell's tip-link complex in the mammalian cochlea.* eLife, 2019. **8**: p. e43473.
15. Ruan, Q., et al., *Topological and developmental expression gradients of Kir2. 1, an inward rectifier K+ channel, in spiral ganglion and cochlear hair cells of mouse inner ear.* Developmental neuroscience, 2009. **30**(6): p. 374-388.
16. Shi, T., et al., *Single-cell transcriptomic profiling of the zebrafish inner ear reveals molecularly distinct hair cell and supporting cell subtypes.* Elife, 2023. **12**: p. e82978.
17. Jean, P., et al., *Single-cell transcriptomic profiling of the mouse cochlea: An atlas for targeted therapies.* Proceedings of the National Academy of Sciences, 2023. **120**(26): p. e2221744120.
18. Kolla, L., et al., *Characterization of the development of the mouse cochlear epithelium at the single cell level.* Nature communications, 2020. **11**(1): p. 2389.
19. Sun, G., et al., *Single-cell transcriptomic atlas of mouse cochlear aging.* Protein & Cell, 2023. **14**(3): p. 180-201.
20. Milon, B., et al., *A cell-type-specific atlas of the inner ear transcriptional response to acoustic*

trauma. Cell reports, 2021. **36**(13).

21. Benkafadar, N., et al., *Transcriptomic characterization of dying hair cells in the avian cochlea.* Cell reports, 2021. **34**(12).
22. Janesick, A.S., et al., *Avian auditory hair cell regeneration is accompanied by JAK/STAT-dependent expression of immune-related genes in supporting cells.* Development, 2022. **149**(8).
23. Baek, S., et al., *Single-cell transcriptome analysis reveals three sequential phases of gene expression during zebrafish sensory hair cell regeneration.* Developmental cell, 2022. **57**(6): p. 799-819. e6.
24. Shrestha, B.R., et al., *Sensory Neuron Diversity in the Inner Ear Is Shaped by Activity.* Cell, 2018. **174**(5): p. 1229-1246 e17.
25. Petitpré, C., et al., *Single-cell RNA-sequencing analysis of the developing mouse inner ear identifies molecular logic of auditory neuron diversification.* Nature communications, 2022. **13**(1): p. 3878.
26. Sun, S., et al., *Hair cell mechanotransduction regulates spontaneous activity and spiral ganglion subtype specification in the auditory system.* Cell, 2018. **174**(5): p. 1247-1263. e15.
27. Longo, S.K., et al., *Integrating single-cell and spatial transcriptomics to elucidate intercellular tissue dynamics.* Nature Reviews Genetics, 2021. **22**(10): p. 627-644.
28. Piwecka, M., N. Rajewsky, and A. Rybak-Wolf, *Single-cell and spatial transcriptomics: deciphering brain complexity in health and disease.* Nature Reviews Neurology, 2023. **19**(6): p. 346-362.
29. Asp, M., et al., *A spatiotemporal organ-wide gene expression and cell atlas of the developing human heart.* Cell, 2019. **179**(7): p. 1647-1660. e19.
30. Farah, E.N., et al., *Spatially organized cellular communities form the developing human heart.* Nature, 2024. **627**(8005): p. 854-864.
31. Yao, Z., et al., *A high-resolution transcriptomic and spatial atlas of cell types in the whole mouse brain.* Nature, 2023. **624**(7991): p. 317-332.
32. Kanemaru, K., et al., *Spatially resolved multiomics of human cardiac niches.* Nature, 2023. **619**(7971): p. 801-810.
33. Li, J., *Single-cell atlas comparison across vertebrates reveals evolution of auditory cell types and mechanisms for hair cell regeneration.* 2024.
34. Peeleman, N., et al., *On the Role of Fibrocytes and the Extracellular Matrix in the Physiology and Pathophysiology of the Spiral Ligament.* Frontiers in Neurology, 2020. **11**.
35. Petitpre, C., et al., *Single-cell RNA-sequencing analysis of the developing mouse inner ear identifies molecular logic of auditory neuron diversification.* Nat Commun, 2022. **13**(1): p. 3878.
36. Sun, G., et al., *Single-cell transcriptomic atlas of mouse cochlear aging.* Protein Cell, 2023. **14**(3): p. 180-201.
37. Petitpré, C., et al., *Neuronal heterogeneity and stereotyped connectivity in the auditory afferent system.* Nature Communications, 2018. **9**(1).
38. Harlow, D.E., et al., *Expression of proteolipid protein gene in spinal cord stem cells and early oligodendrocyte progenitor cells is dispensable for normal cell migration and myelination.* Journal of Neuroscience, 2014. **34**(4): p. 1333-1343.
39. Chew, H., V.A. Solomon, and A.N. Fonteh, *Involvement of lipids in Alzheimer's disease pathology and potential therapies.* Frontiers in physiology, 2020. **11**: p. 598.
40. Rask-Andersen, H., et al., *Human cochlea: anatomical characteristics and their relevance for*

cochlear implantation. The Anatomical Record: Advances in Integrative Anatomy and Evolutionary Biology, 2012. **295**(11): p. 1791-1811.

41. Chonko, K.T., et al., *Atoh1 directs hair cell differentiation and survival in the late embryonic mouse inner ear.* Developmental biology, 2013. **381**(2): p. 401-410.
42. Pirvola, U., et al., *FGF/FGFR-2 (IIIb) signaling is essential for inner ear morphogenesis.* Journal of Neuroscience, 2000. **20**(16): p. 6125-6134.
43. Guo, J., C. Walss-Bass, and R.F. Ludueña, *The β isotypes of tubulin in neuronal differentiation.* Cytoskeleton, 2010. **67**(7): p. 431-441.
44. Ahmed, M., J. Xu, and P.-X. Xu, *EYA1 and SIX1 drive the neuronal developmental program in cooperation with the SWI/SNF chromatin-remodeling complex and SOX2 in the mammalian inner ear.* Development, 2012. **139**(11): p. 1965-1977.
45. Breuskin, I., et al., *Glial but not neuronal development in the cochleo-vestibular ganglion requires Sox10.* Journal of neurochemistry, 2010. **114**(6): p. 1827-1839.
46. Gulati, G.S., et al., *Profiling cell identity and tissue architecture with single-cell and spatial transcriptomics.* Nature Reviews Molecular Cell Biology, 2024: p. 1-21.
47. Jiang, L., et al., *Advances in gene therapy hold promise for treating hereditary hearing loss.* Molecular Therapy, 2023. **31**(4): p. 934-950.
48. Sennaroğlu, L. and M.D. Bajin, *Classification and current management of inner ear malformations.* Balkan medical journal, 2017. **34**(5): p. 397-411.
49. Huang, S., et al., *Gene4HL: An Integrated Genetic Database for Hearing Loss.* Frontiers in Genetics, 2021. **12**.
50. Hao, Y., et al., *Dictionary learning for integrative, multimodal and scalable single-cell analysis.* Nat Biotechnol, 2024. **42**(2): p. 293-304.
51. Jin, S., et al., *Inference and analysis of cell-cell communication using CellChat.* Nature Communications, 2021. **12**(1).
52. Qiu, X., et al., *Reversed graph embedding resolves complex single-cell trajectories.* Nature Methods, 2017. **14**(10): p. 979-982.
53. Alquicira-Hernandez, J. and J.A.-O. Powell, *Nebulosa recovers single-cell gene expression signals by kernel density estimation.* Bioinformatics, 2021. **37**(16): p. 2485-2487.
54. Li, J., et al., *Dynamic changes in cis-regulatory occupancy by Six1 and its cooperative interactions with distinct cofactors drive lineage-specific gene expression programs during progressive differentiation of the auditory sensory epithelium.* Nucleic acids research, 2020. **48**(6): p. 2880-2896.
55. Sun, Y., et al., *Single-cell transcriptomic landscapes of the otic neuronal lineage at multiple early embryonic ages.* Cell Reports, 2022. **38**(12).
56. Chen, T., et al., *The genome sequence archive family: toward explosive data growth and diverse data types.* Genomics, Proteomics and Bioinformatics, 2021. **19**(4): p. 578-583.
57. *Database resources of the national genomics data center, China national center for bioinformation in 2022.* Nucleic Acids Research, 2022. **50**(D1): p. D27-D38.

Figure Legends

Figure 1

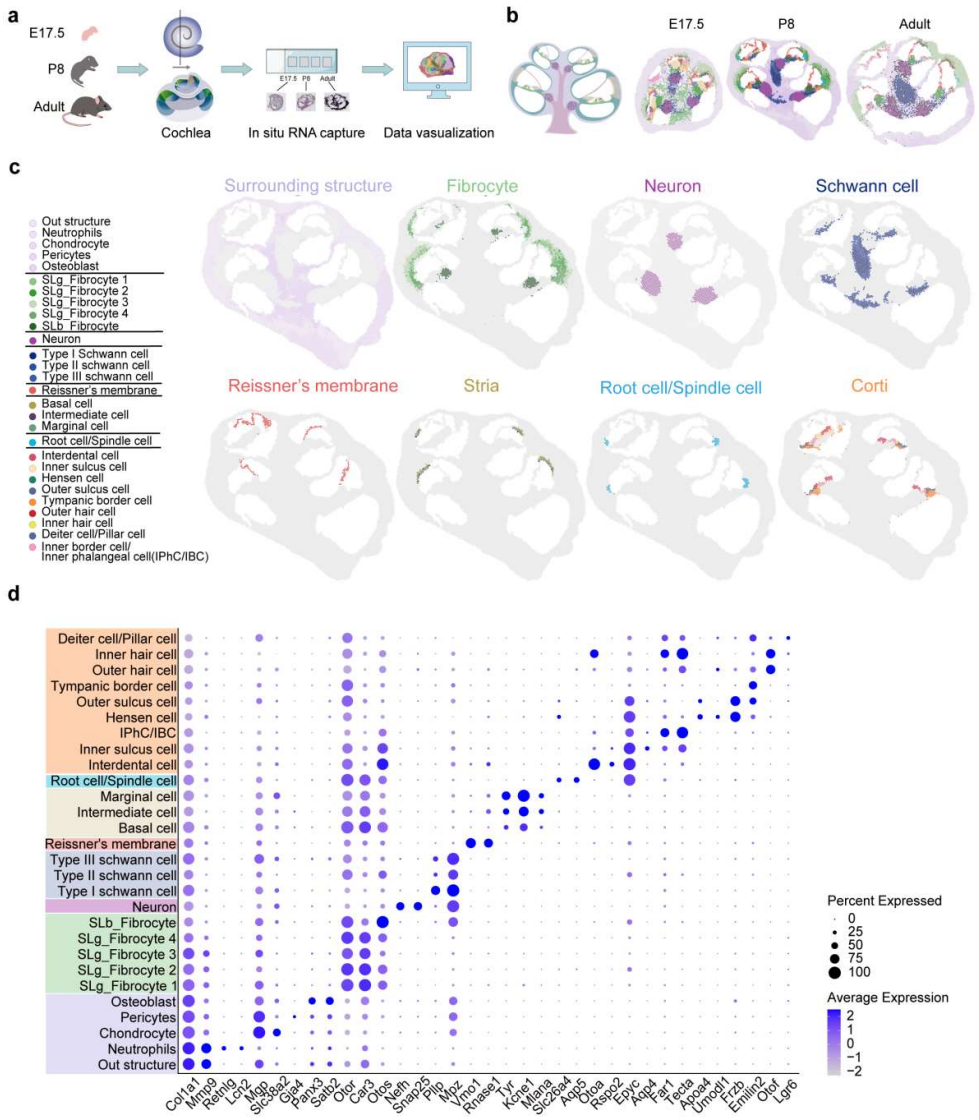

Fig. 1 Spatial single-cell atlas of developing and adult cochlea. (**a**) The work flow of spatial transcriptomic assay for mouse cochlea at three stages (E17.5, P8, 2M). (**b**) Left, the diagram of cochlea depicting the cross-section direction. Right, visualization of spatial RNA-seq barcoded spots colored by cell types for the three developmental stages. (**c**) Spatial single cell types in the P8 cochlea cross-section. Eight major groups

of cell types were shown, respectively SLg: spiral ligament, SLb: spiral limbus. (**d**) Bubble plot analysis of the top differentially expressed genes for each cell types in the P8 cochlea. The size of the dots represents the percentage of cells in the clusters expressing the genes and the color intensity represents the average expression levels of the gene in that cluster.

Figure 2

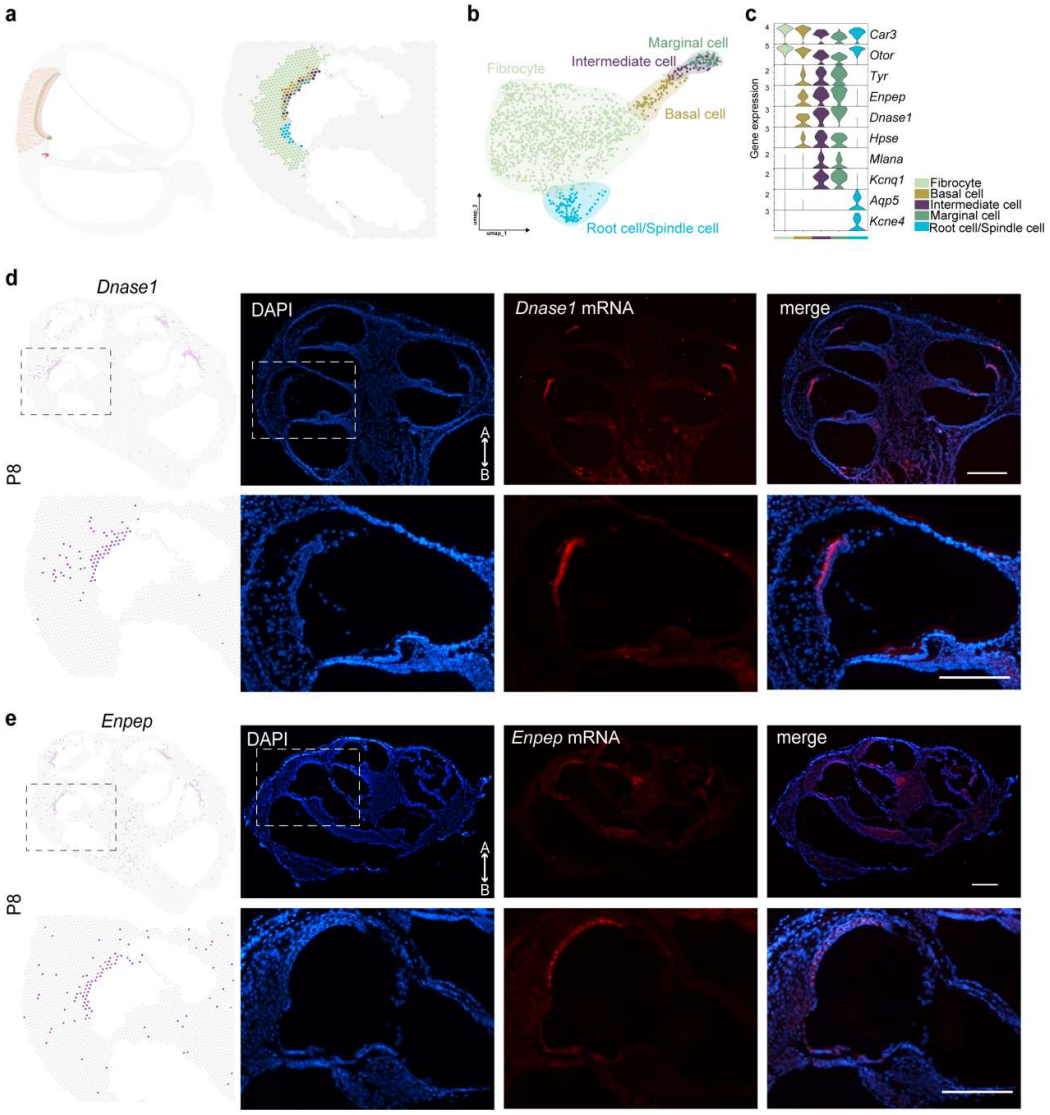

Fig. 2 Spatial analyses of lateral wall cell subtypes. (**a**) Left, the diagram of the cochlea highlighting main cell types from the lateral wall structure. Right, the spatial distribution of lateral wall cell subtypes at P8 cochlea. (**b**) UMAP plot showing the cell types in lateral wall (LW) in the P8 datasets. (**c**) Violin plots showing the differential expression genes to distinguish each LW cell type. (**d**) Upper, spatial dot painting for *Dnase1* gene expression on spatial chip and its RNA *in situ* detection (red) on P8 whole-cochlea cryosection. DAPI is labeled in blue. Bottom, magnified view of selected

region above, as indicated by white dashed box above. (**e**) Upper, spatial painting of *Enpep* gene on chips and its RNA *in situ* validation (red) on the P8 whole-cochlea cryosection. DAPI is labeled in blue. Bottom, magnified view of selected region in above dashed box. A, apical; B, basal. All scale bar equals to 200 μm.

Figure 3

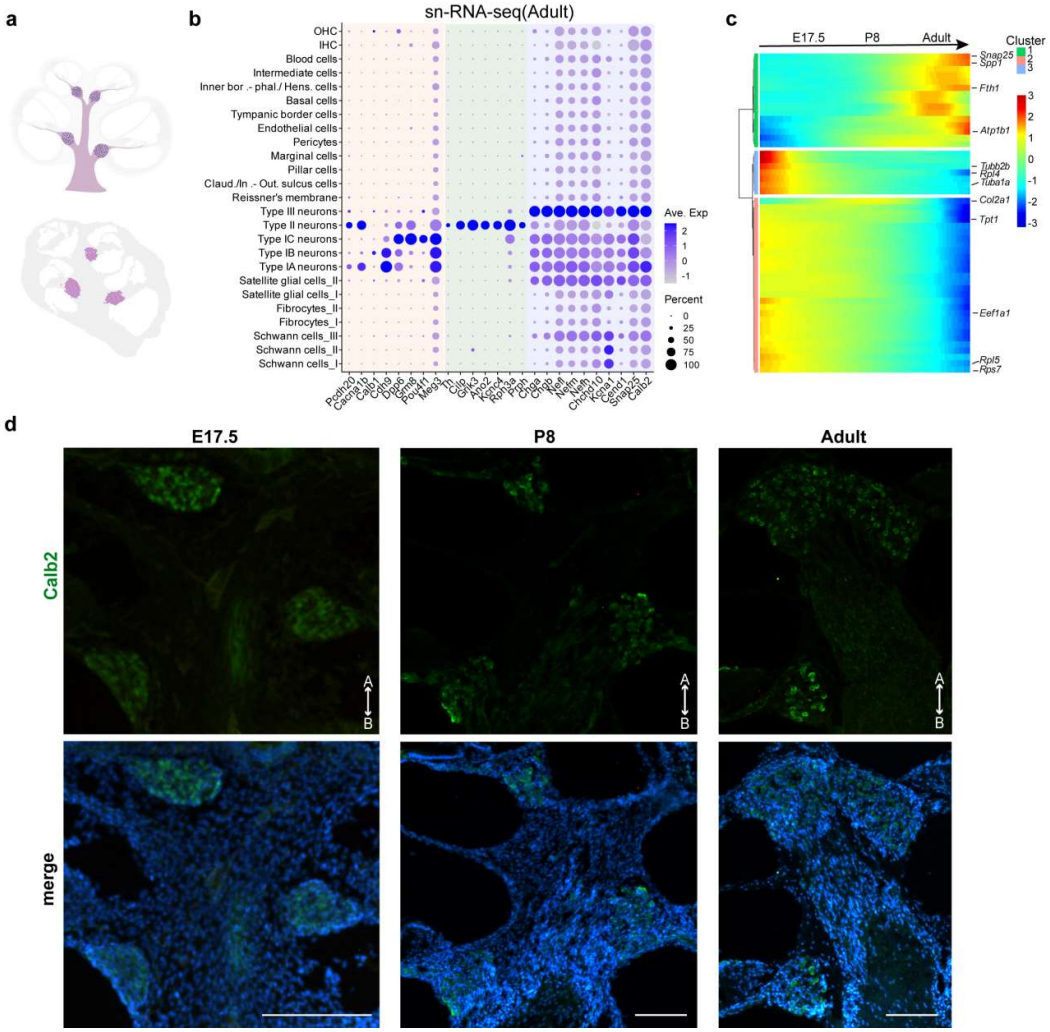

Fig. 3 Temporal dynamics of gene expression in spiral ganglion neurons during cochlear development. (**a**) Upper, the diagram of neuronal system in cross-section of cochlea. Bottom, the spatial distribution of neuron cells at P8 cochlea. (**b**) Bubble plot showing the differential expression of 25 neuron markers representing each SGN subtype identified in previous single-cell or single-nucleus RNA-seq dataset. OHC, outer hair cell IHC, inner hair cell; IPhC/IBC, inner phalangeal cell/inner border cell; ISC/OSC/CC, inner sulcus cell/outer sulcus cell/Claudius cell. The size of the dots represents the percentage of cells in the clusters expressing the genes and the color

intensity represents the average expression levels of the gene in that cluster. (**c**) Heatmap showing the pseudotime analysis for neuron cells from E17.5, P8 and adult dataset, with the top 10 upregulated genes along the differentiation of each branch. (**d**) Immunostaining of Calb2 (green) on the E17.5, P8, adult cochlea cross-section. DAPI is labeled in blue. A, apex; B, base. Scale bar equals to 200 μm.

Figure 4

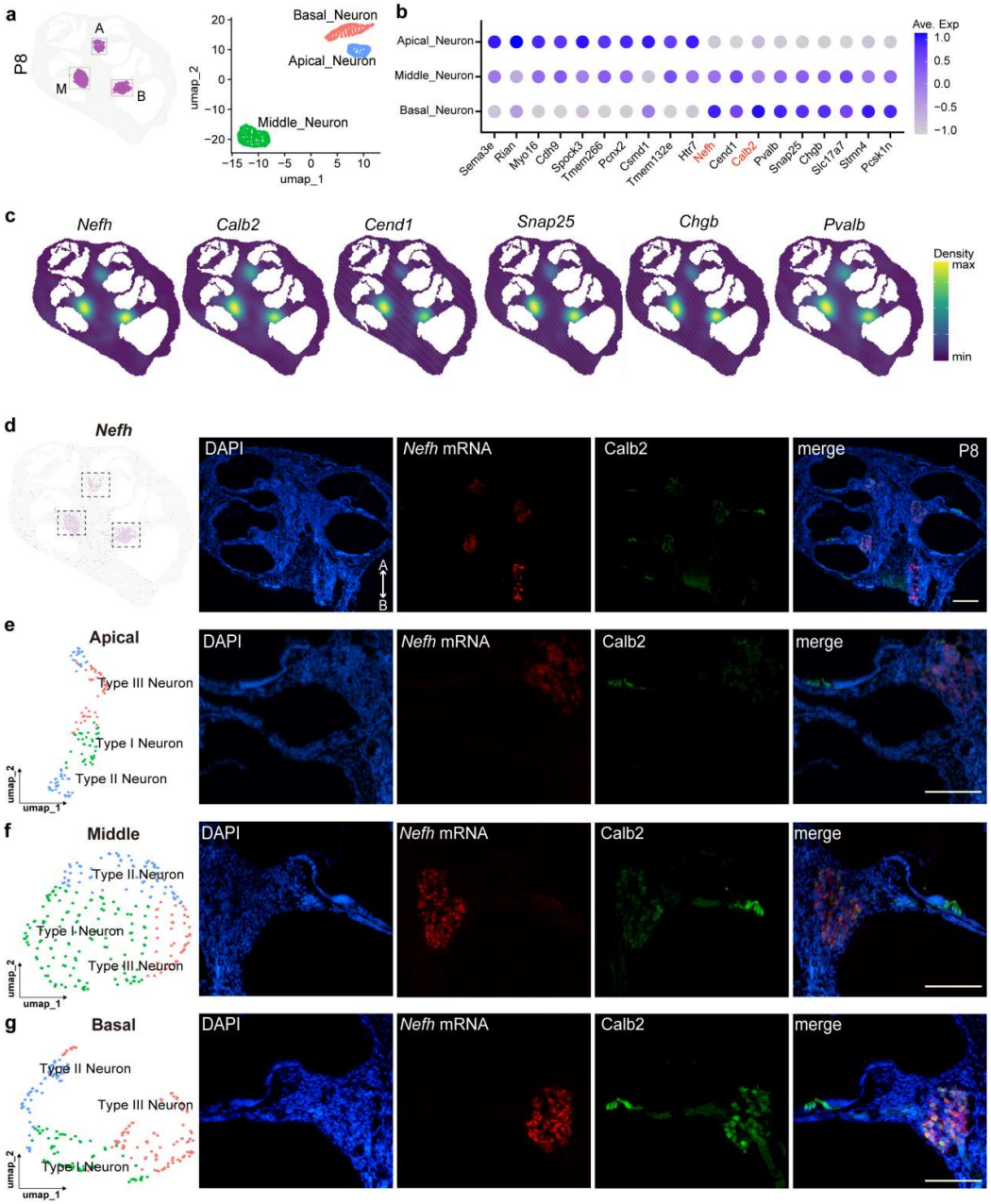

Fig. 4 Spatial differential analysis reveals gradients of neuronal gene expression from apical to basal SGNs. (**a**) Left, spatial painting of spiral ganglion neurons (SGNs) at P8 cochlea. The rectangular boxes with different colors indicate three different regions. A, apical; M, middle; B, basal. Right, UMAP plot showing the apical middle and basal neurons extracted from P8 cochlea in the left. (**b**) Bubble plot showing the

expression level of the 17 gradient genes representing two patterns (decreasing or increasing expression pattern from apex to base). The genes which were confirmed by RNA *in situ* or immunofluorescent staining assay were labeled in red. The size of the dots represents the percentage of cells in the clusters expressing the genes and the color intensity represents the average expression levels of the gene in that cluster. (**c**) Density plots showing the spatial expression of *Nefh*, *Calb2*, *Cend1*, *Snap25*, *Chgb* and *Pvalb*, on P8 cochlea section chip. (**d**) Left, spatial expression of *Nefh* on P8 cochlea section, black dotted boxes labeled the neuron cells from apical, middle, and basal region, respectively. Right, immunostaining of Calb2 (green) and RNA *in situ* detection of *Nefh* mRNA (red) on P8 cochlea cross-section. DAPI is labeled in blue. A, apical; B, basal. (**e-g**) Left, UMAP plots showing the neuronal cell subtypes from apical, middle and basal region, respectively. Right, magnified view of neuron cell staining in apex region (**e**), middle (**f**) and basal (**g**) regions, respectively. All scale bar equals to 200 μm.

Figure 5

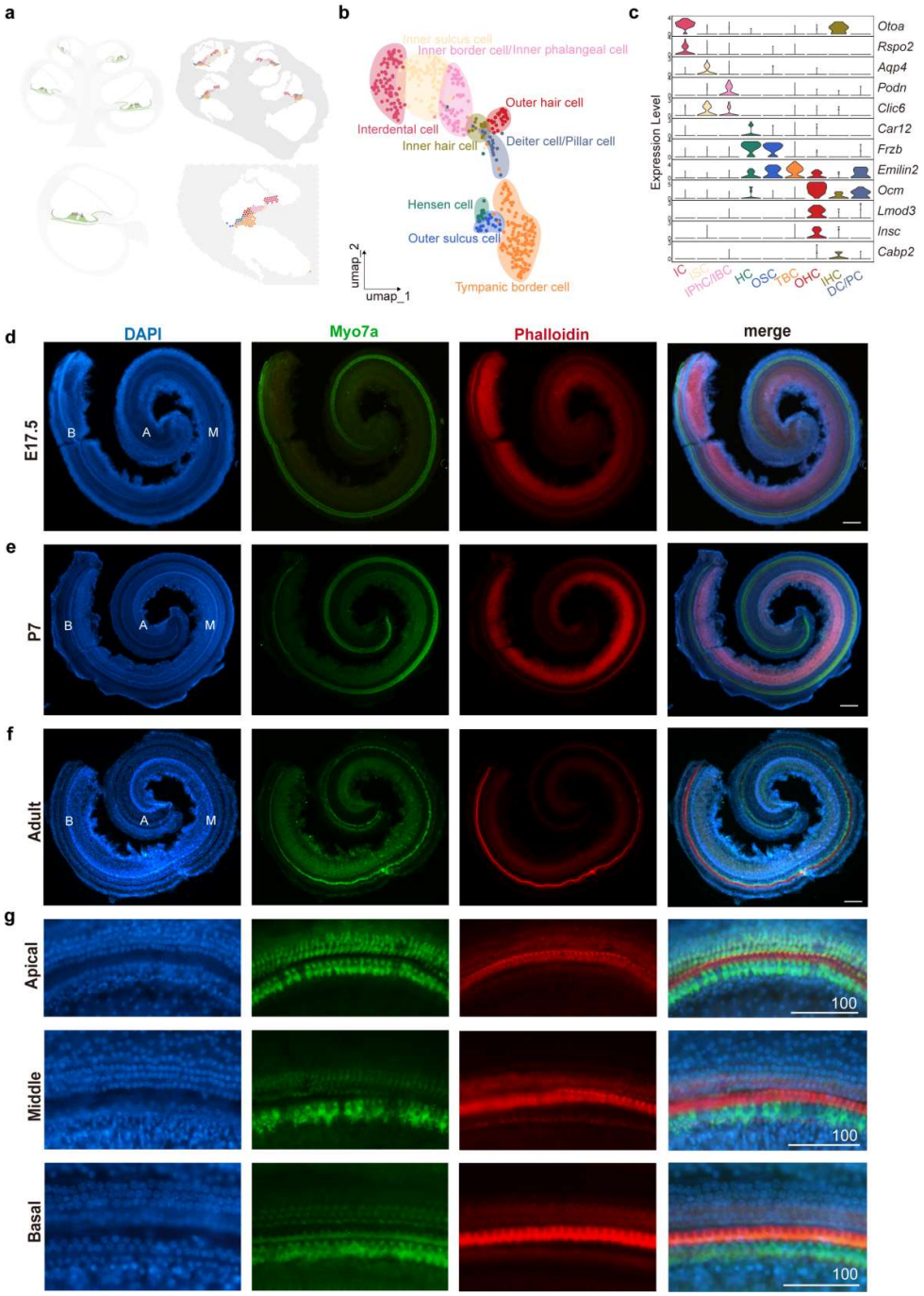

Fig. 5 Spatiotemporal analysis for the organ of Corti cell. (**a**) Upper left, the diagram of cochlea cross-section highlighting the cells from the organ of Corti (OC). Upper right, spatial painting of cell clusters from OC identified in P8 cochlea. Bottom left, magnified

view of (**a**, Upper left) to show the cells in OC. Bottom right, magnified view of (**a**, Upper right) to show the spatial painting of cell clusters from OC. Spots were colored by identity. (**b**) UMAP plot showing the cell clusters from OC colored by cell types, including interdental cell (IC), inner sulcus cell (ISC), inner phalangeal cell/inner border cell (IPhC/IBC), Hensen's cell (HC), outer sulcus cell (OSC), tympanic border cell (TBC), outer hair cell (OHC), inner hair cell (IHC) and Deiter cell_pillar cell (DC_PC). (**c**) Violin plots showing expression levels for a subset of genes used to classify cell types in (**b**). (**d-f**) Immunostaining of hair cells for the whole-mount cochlea at E17.5 (**d**), P8 (**e**) and adult (**f**). Myo7a is labeled in green; phalloidin, red; DAPI, blue. Scale bars equal to 200 μm. (**g**) Magnified view of (**f**) showing apical (upper), middle (middle), and basal (bottom) regions of adult cochlea, respectively. A, apical; M, middle; B, basal. Scale bars equal to 100 μm

Figure 6

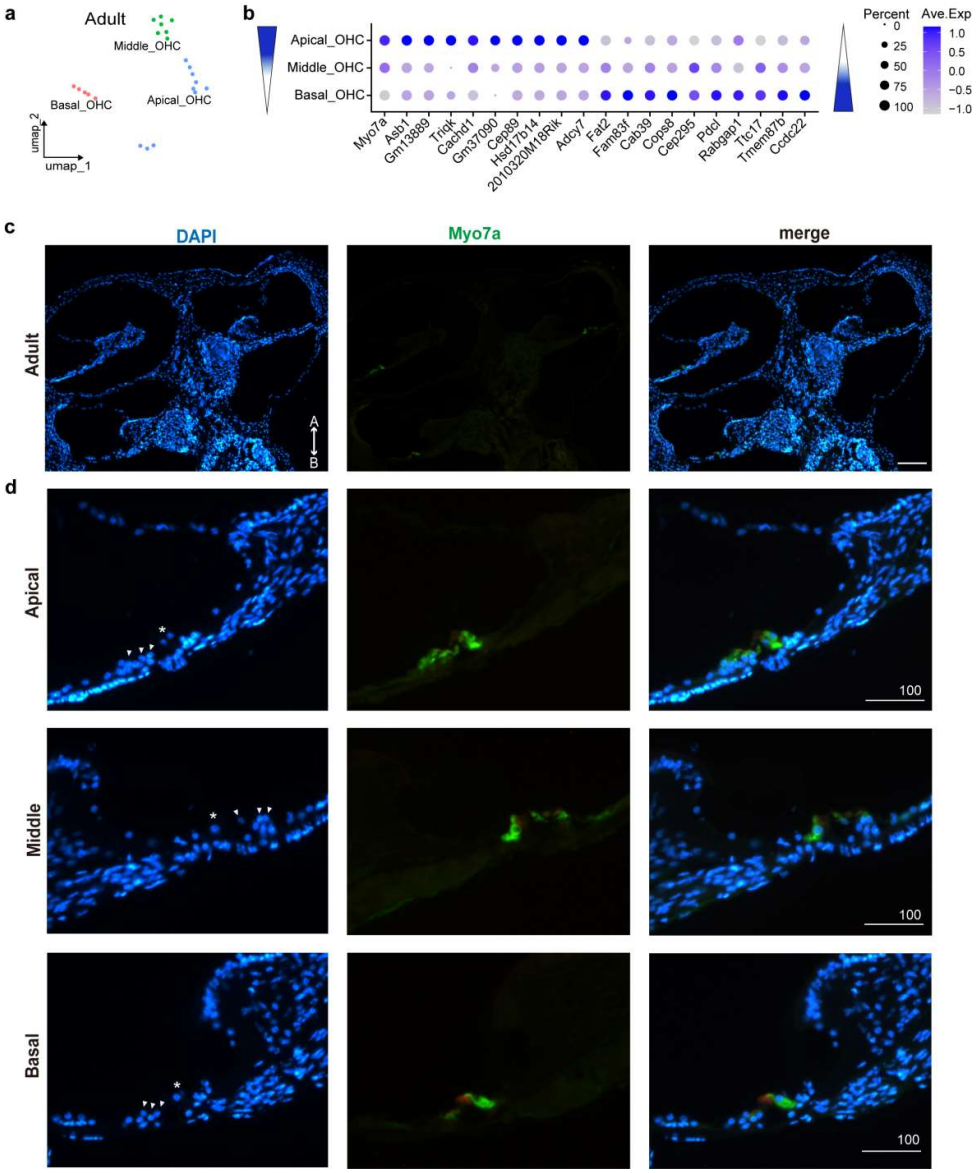

Fig. 6 Spatial differential analysis reveals gene expression gradients of OHCs from apex to base. (**a**) UMAP plot showing OHCs extracted from apical, middle and basal regions of P8 cochlea, colored by regions. (**b**) Bubble plot showing a number of gene expressions in OHCs with two gradient patterns (Apex-to-base decreasing or increasing expression). (**c**) Immunostaining of myo7a (green) on P8 cochlea section. DAPI is labeled in blue. Scale bar equals to 200 μm. (**d**) Magnified view of (**c**) to show staining

of hair cell in apex region (upper), middle (middle) and basal regions (bottom), respectively. The triangles indicate OHCs and the stars indicate the IHCs. Scale bars equal to 100 μm. A, apical; B, basal; IHC, inner hair cell; OHC, outer hair cell.

Figure 7

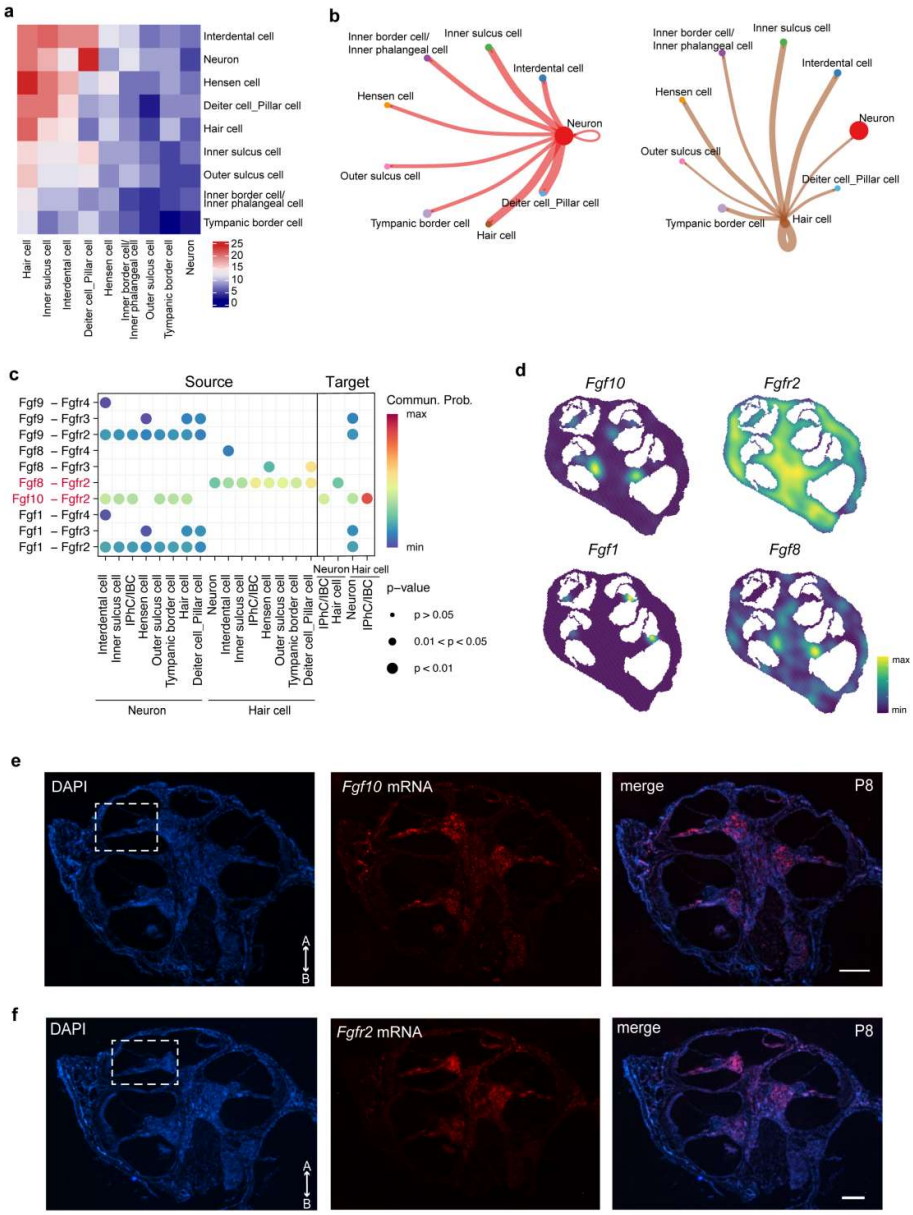

Fig. 7 Developmental dynamics of cell-cell communication network between cell clusters from the organ of Corti. (**a**) Heatmap showing the number of ligand-receptor pairs evaluated by cellchat for neuron cell and cell clusters from organ of Corti (OC) at P8. (**b**) Left, number of significant ligand-receptor pairs between cell clusters from OC at P8, with the neuron cell as a hub. Right, number of significant ligand-receptor pairs

between cell clusters from OC at P8, with hair cells as a hub. The edge width is proportional to the indicated number of ligand-receptor pairs. (**c**) Bubble plots showing ligand-receptor pairs of FGF signaling pathway between neuron cell and other cell clusters from OC. The size of dots represents the significance and the color represents the communication probability. (**d**) Spatial dense plots showing the expression level of *Fgf10*, *Fgfr2*, *Fgf1* and *Fgf8* at P8 cochlea section. (**e**,**f**) RNA *in situ* validating the expression of *Fgf10* mRNA (**e**) and *Fgfr2* mRNA (**f**) on P8 cochlea sections. The magnified views of dash-boxed regions are seen in Fig. S7. Scale bar equals to 200 μm. A, apical; B, basal.

Figure 8

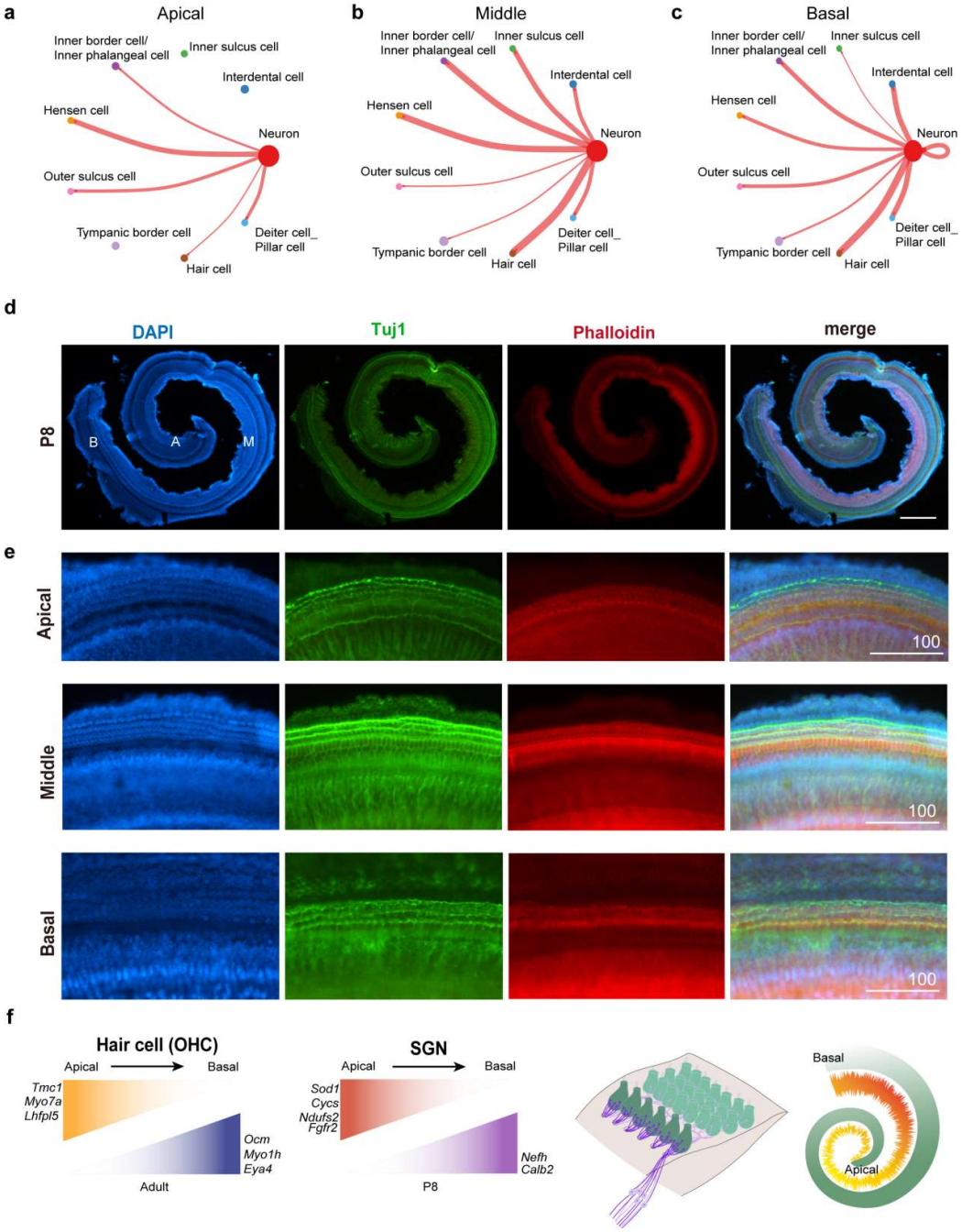

Fig. 8 Spatial cell-cell communication network from apex to base. (a-c) Number of significant ligand-receptor pairs between neuron cell and other cell clusters from OC located in the apical, middle and basal regions at P8, respectively. The edge width is proportional to the indicated number of ligand-receptor pairs. (**d**) The whole-mount

immunostaining of Tuj1 (green) and phalloidin (red) on P8 cochlea. DAPI, blue. Scale bar equals to 200 μm. (**e**) Magnified view of (**d**) to show neuronal connections and projections in apical (upper), middle (middle), and basal (bottom) regions, respectively. (**f**) Schematic representation illustrating the gradient patterning observed in hair cells and SGNs, highlighting a potential molecular mechanism underlying the tonotopic organization along the cochlear axis. A, apical; M, middle; B, basal.

Figure S1

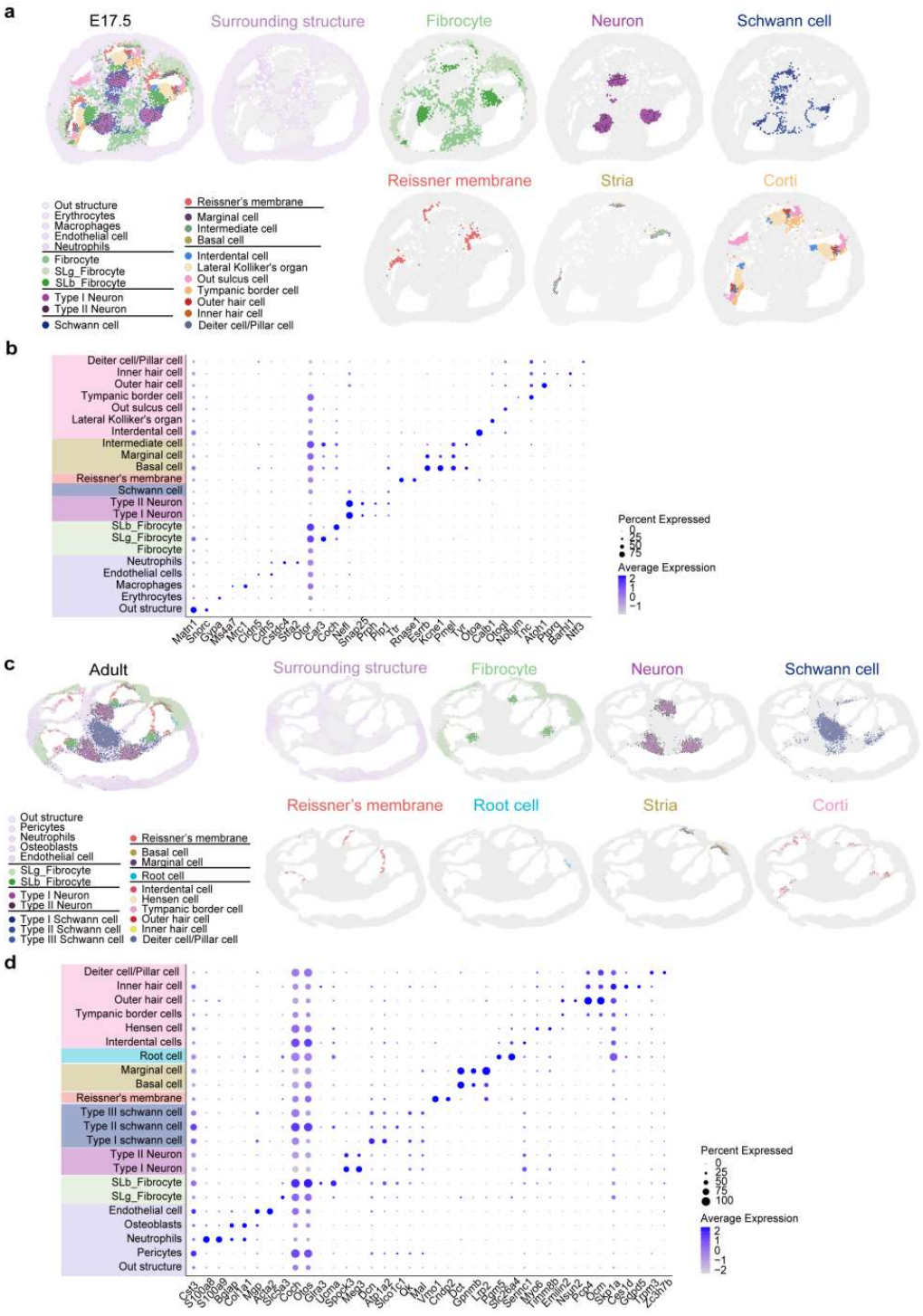

Fig. S1 Spatial single-cell atlas of developing and adult cochlea. (**a**) Spatial single cell types on the E17.5 cochlea cross-section. Eight major groups of cell types were

shown, respectively. SLg: spiral ligament, SLb: spiral limbus. (**b**) Bubble plot analysis of the top differentially expressed genes for each cell types in the E17.5 cochlea. The size of the dots represents the percentage of cells in the clusters expressing the gene and the color intensity represents the average expression levels of the gene in that cluster. (**c**) Spatial single cell types on the adult cochlea cross-section. Eight major groups of cell types were shown, respectively. (**d**) Bubble plot analysis of the top differentially expressed genes for each cell types on the adult cochlea. The size of the dots represents the percentage of cells in the clusters expressing the gene and the color intensity represents the average expression level of the gene in that cluster.

Figure S2

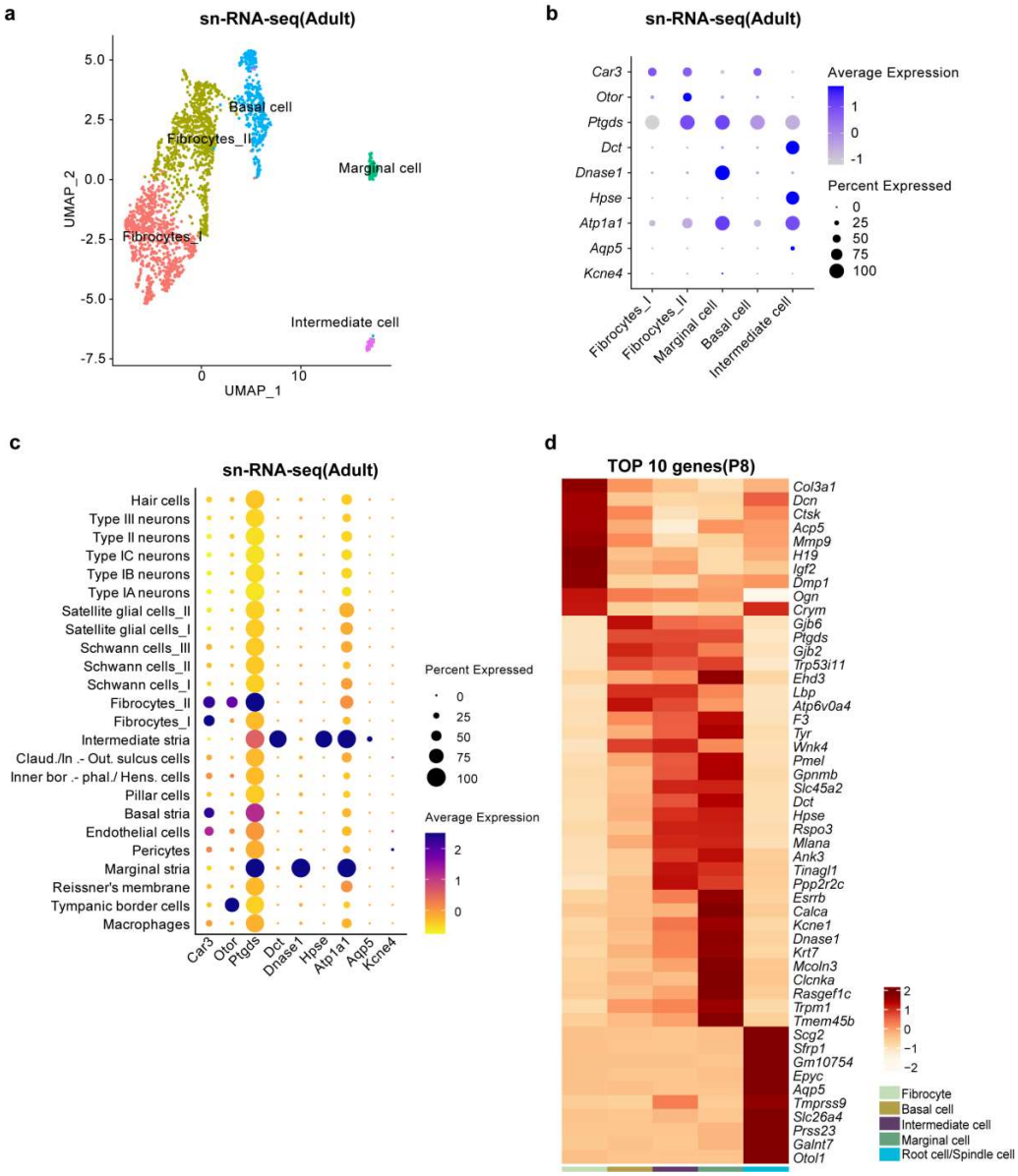

Fig. S2 Spatial analyses of lateral wall cell subtypes. (**a**) UMAP plot showing the lateral wall cells in the snRNA-seq colored by cell types. (**b**, **c**) Bubble plot showing the markers from Fig. 2c in the snRNA-seq dataset of cochlea. The size of the dots represents the percentage of cells in the clusters expressing the genes and the color intensity represents the average expression levels of the gene in that cluster. (**d**) Heatmap showing the expression level of the top 10 differential gene markers

classifying the cell types from the lateral wall in the P8 spatial dataset.

Figure S3-1

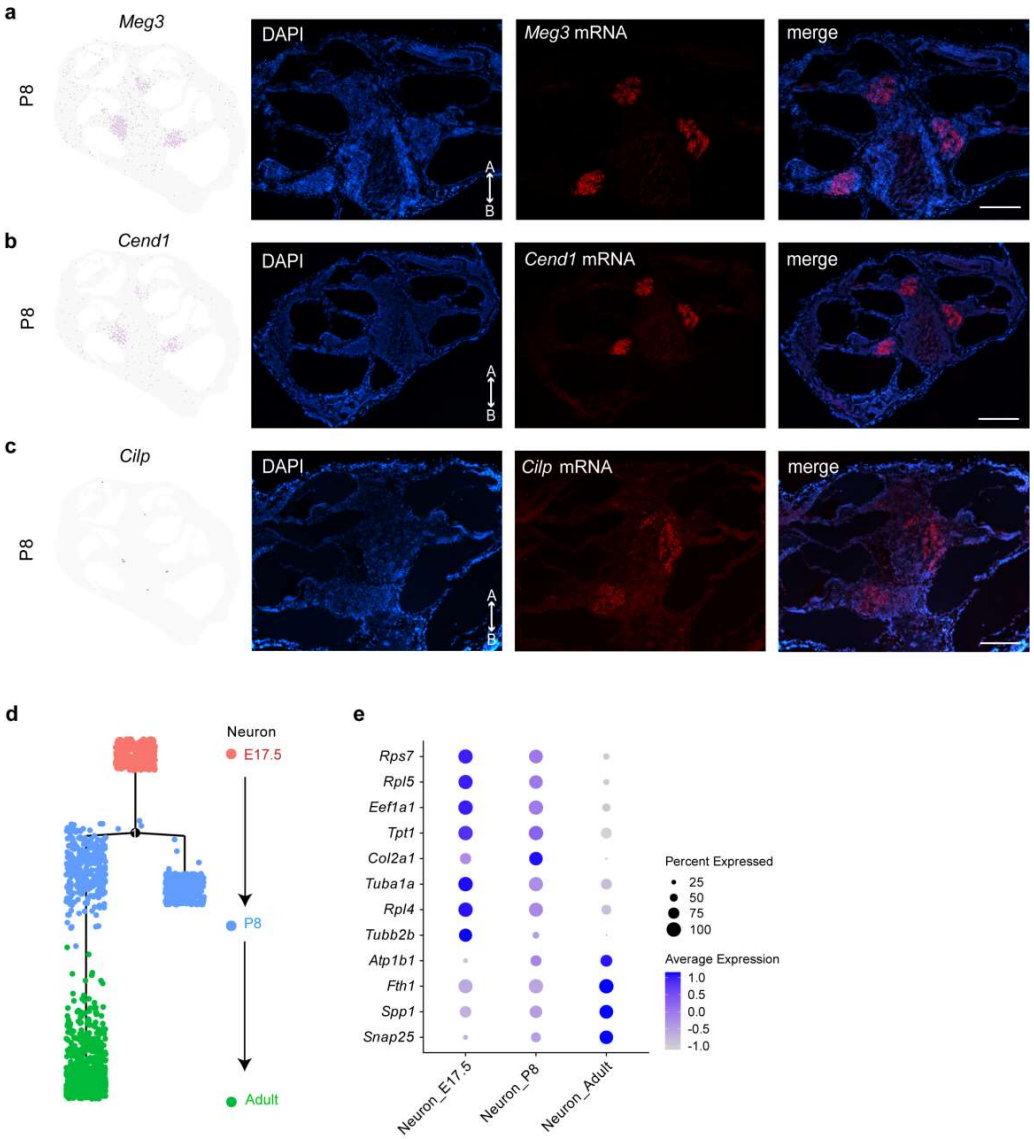

Fig. S3-1 Spatial dynamics of gene expression in spiral ganglion neurons. (**a, b**) Left, spatial expression of *Meg3* (**a**) and *Cend1* (**b**) on P8 cochlea spatial section chip. Right, RNA *in situ* detection of *Meg3* and *Cend1* mRNA on P8 cochlea section. Scale bar equals to 200 μm. (**c**) Dendrogram recapitulating the branched trajectory of the developing SGNs (E17.5, P8, and adult) based on the transcriptional similarity of pseudotime-ordered cells. (**d**) Bubble plot showing the differential expression of a set of genes in neuron cells at different development stages. The size of the dots represents

the percentage of cells in the clusters expressing the genes and the color intensity represents the average expression levels of the gene in that cluster. A, apical; B, basal.

Figure S3-2

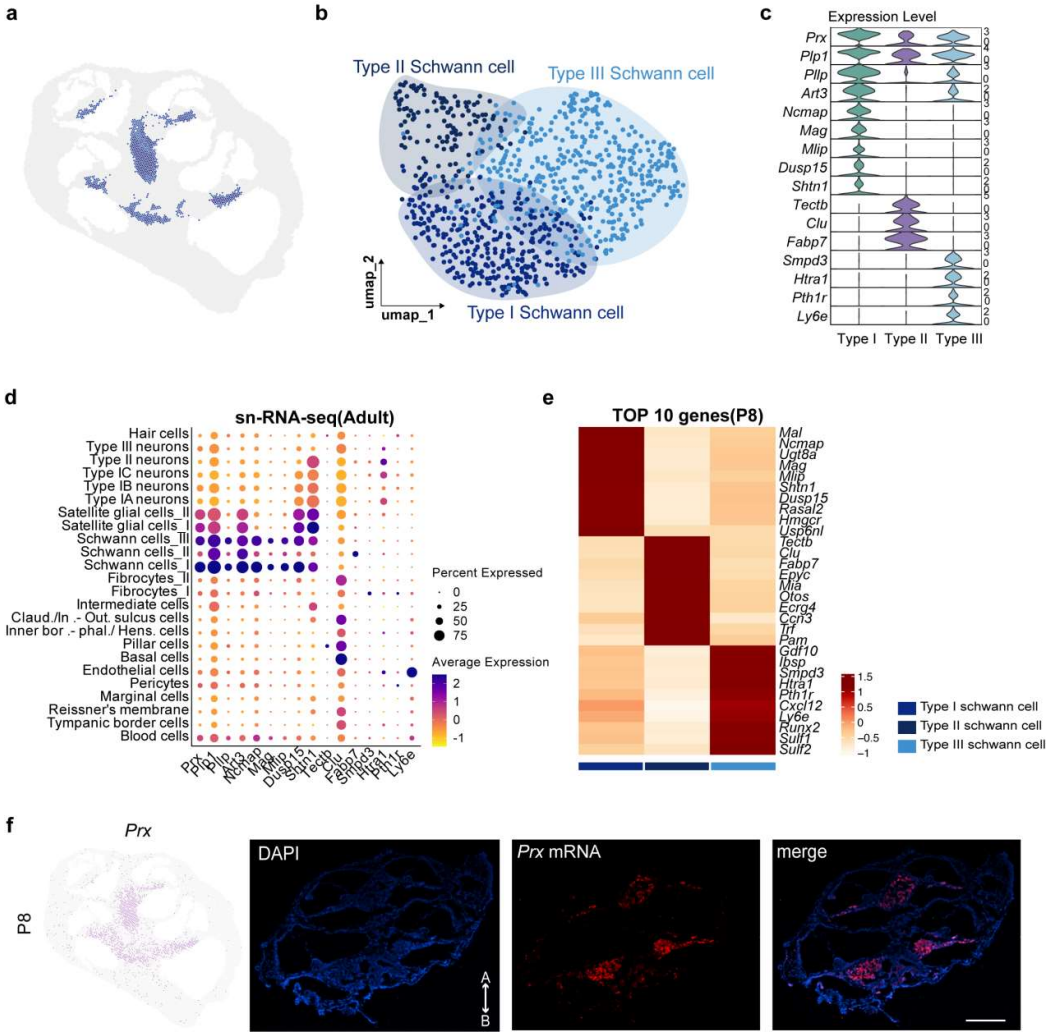

Fig. S3-2 Spatial expression pattern of Schwann cell subtypes. (**a**) Spatial distribution of Schwann cell at P8 cochlea. (**b**) UMAP plot showing the subtypes of Schwann cell at P8 cochlea colored by subtypes. (**c**) Violin plots showing the expression level of a set of genes classifying subgroups of the Schwann cell. (**d**) Bubble plot showing the expression level of genes from (**c**) in snRNA-seq dataset. The size of the dots represents the percentage of cells in the clusters expressing the genes and the color intensity represents the average expression levels of the gene in that cluster. (**e**) Heatmap showing the top 10 genes which were differentially expressed in the three

subclusters of Schwann cell in P8 spatial dataset. (**f**) Left, spatial expression of *Prx* at P8 cochlea, which specifically expressed in Schwann cell. Right, RNA *in situ* detection of *Prx* mRNA on P8 cochlea section. Scale bar equals to 200 μm. A, apical; B, basal.

Figure S4

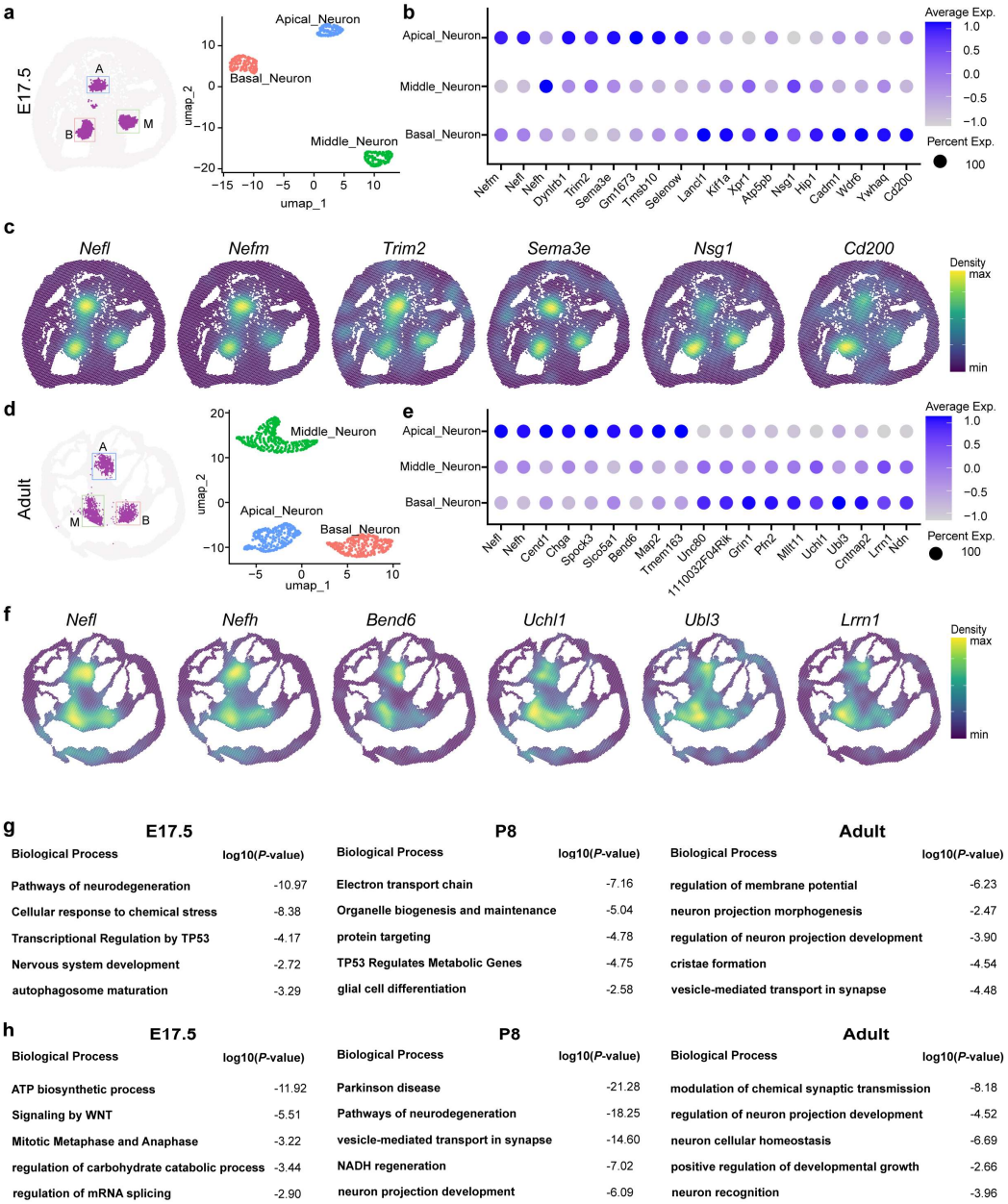

g

E17.5 Biological Process	log10(*P*-value)	P8 Biological Process	log10(*P*-value)	Adult Biological Process	log10(*P*-value)
Pathways of neurodegeneration	-10.97	Electron transport chain	-7.16	regulation of membrane potential	-6.23
Cellular response to chemical stress	-8.38	Organelle biogenesis and maintenance	-5.04	neuron projection morphogenesis	-2.47
Transcriptional Regulation by TP53	-4.17	protein targeting	-4.78	regulation of neuron projection development	-3.90
Nervous system development	-2.72	TP53 Regulates Metabolic Genes	-4.75	cristae formation	-4.54
autophagosome maturation	-3.29	glial cell differentiation	-2.58	vesicle-mediated transport in synapse	-4.48

h

E17.5 Biological Process	log10(*P*-value)	P8 Biological Process	log10(*P*-value)	Adult Biological Process	log10(*P*-value)
ATP biosynthetic process	-11.92	Parkinson disease	-21.28	modulation of chemical synaptic transmission	-8.18
Signaling by WNT	-5.51	Pathways of neurodegeneration	-18.25	regulation of neuron projection development	-4.52
Mitotic Metaphase and Anaphase	-3.22	vesicle-mediated transport in synapse	-14.60	neuron cellular homeostasis	-6.69
regulation of carbohydrate catabolic process	-3.44	NADH regeneration	-7.02	positive regulation of developmental growth	-2.66
regulation of mRNA splicing	-2.90	neuron projection development	-6.09	neuron recognition	-3.96

Fig. S4. Spatial differential analyses of neuronal expressing genes from apex to base. (**a**) Left, spatial distribution of neuron cells at E17.5 cochlea section chip, divided by rectangular boxes with different colors (three regions: A, apical; M, middle; B, basal). Right, UMAP plot showing the apical, middle and basal neurons extracted from E17.5 cochlea as shown on the left, as indicated by different colors. (**b**) Bubble plot showing the expression levels of the 19 genes in neuron cells from the three regions on E17.5

cochlea section, representing two gradient patterns (apex-to-base decreasing and increasing expression). (**c**) Density plots showing the spatial expression of *Nefl*, *Nefm*, *Trim2*, *Sema3e*, *Nsg1* and *Cd200*, on E17.5 cochlea section. (**d**) Left, spatial distribution of neuron cells on adult cochlea section chip, divided by rectangular boxes with different colors. Right, UMAP plot showing the apical, middle and basal neurons extracted from adult cochlea spatial data as shown on the left. (**e**) Bubble plot showing the gradient expression of the 19 genes in neuron cells from the three regions on adult cochlea section, representing two gradient patterns (apex-to-base decreasing and increasing expression). (**f**) Density plots showing the spatial expression levels of *Nefl*, *Nefh*, *Bend6*, *Uchl1, Ubl3 and Lrrn1*, on adult cochlea sections. (**g**,**h**) GO functional analysis of two classes of gradient genes, with apex-to-base decreasing **(g)** and increasing expression **(h)**, respectively**.** A, apical; M, middle; B, basal.

Figure S5

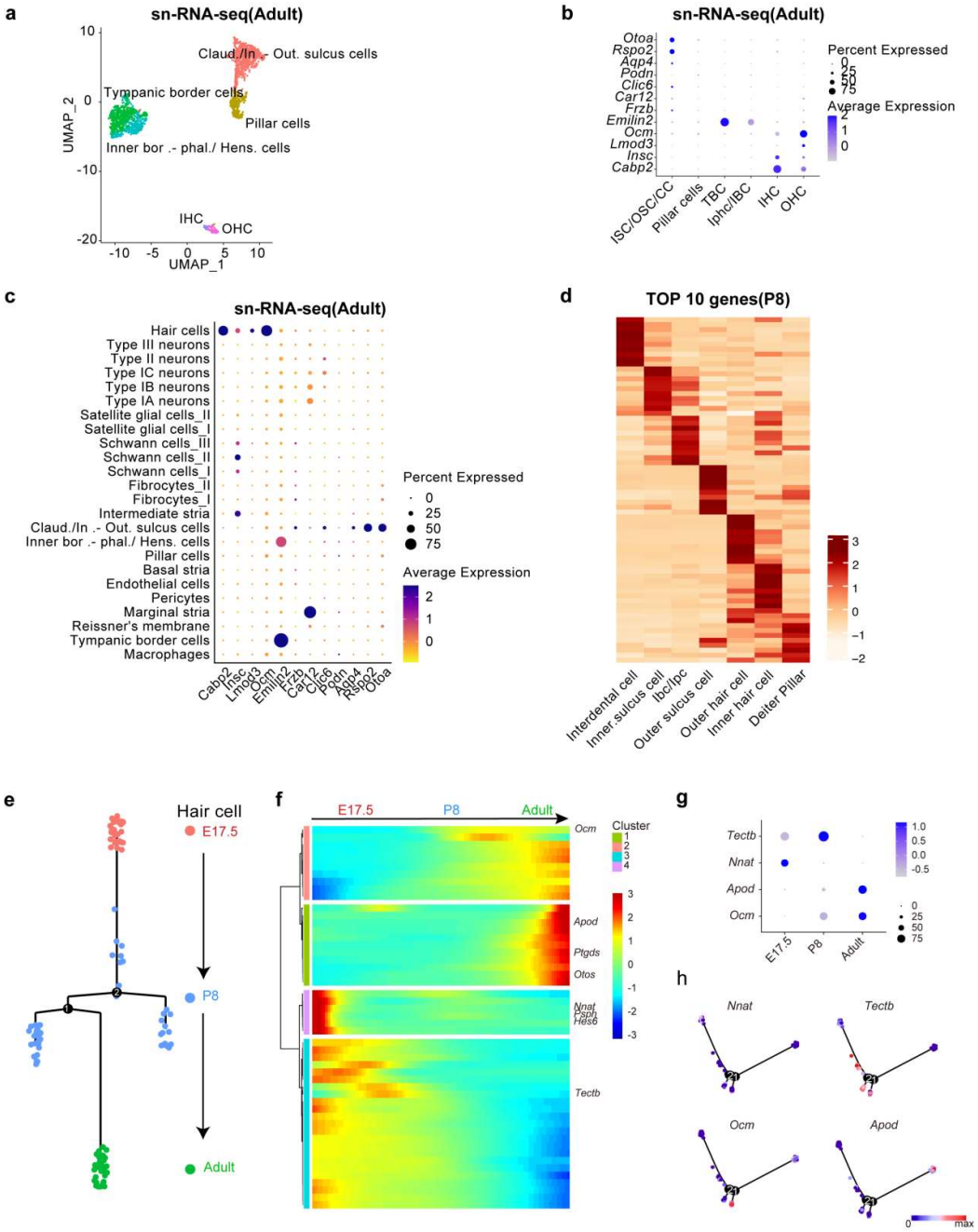

Fig. S5. Spatiotemporal analyses of cells from the organ of Corti. (**a**) UMAP plot for cells from OC group in our previous single nucleus RNA-seq dataset. (**b**, **c**) Bubble plot showing the expression levels of the marker genes from Fig. 5c in the snRNAseq dataset of cochlea. The size of the dots represents the percentage of cells in the clusters

expressing the genes and the color intensity represents the average expression level of the gene in that cluster. (**d**) Heatmap showing the expression levels of the top 10 markers classifying the cell types from the organ of Corti in the P8 dataset. (**e**) Dendrogram recapitulating the branched trajectory of the developing OHCs (E17.5, P8, and adult) based on the transcriptional similarity of pseudotime-ordered cells. (**f**) Heatmap showing overview analysis of the different trajectories, together with the top 50 up-regulated genes along the differentiation of each branch. (**g**) Bubble plot showing the differential expression of a set of genes in hair cells at different development stages. (**h**) Plots showing the expression of different genes in different hair cell trajectories.

Figure S6-1

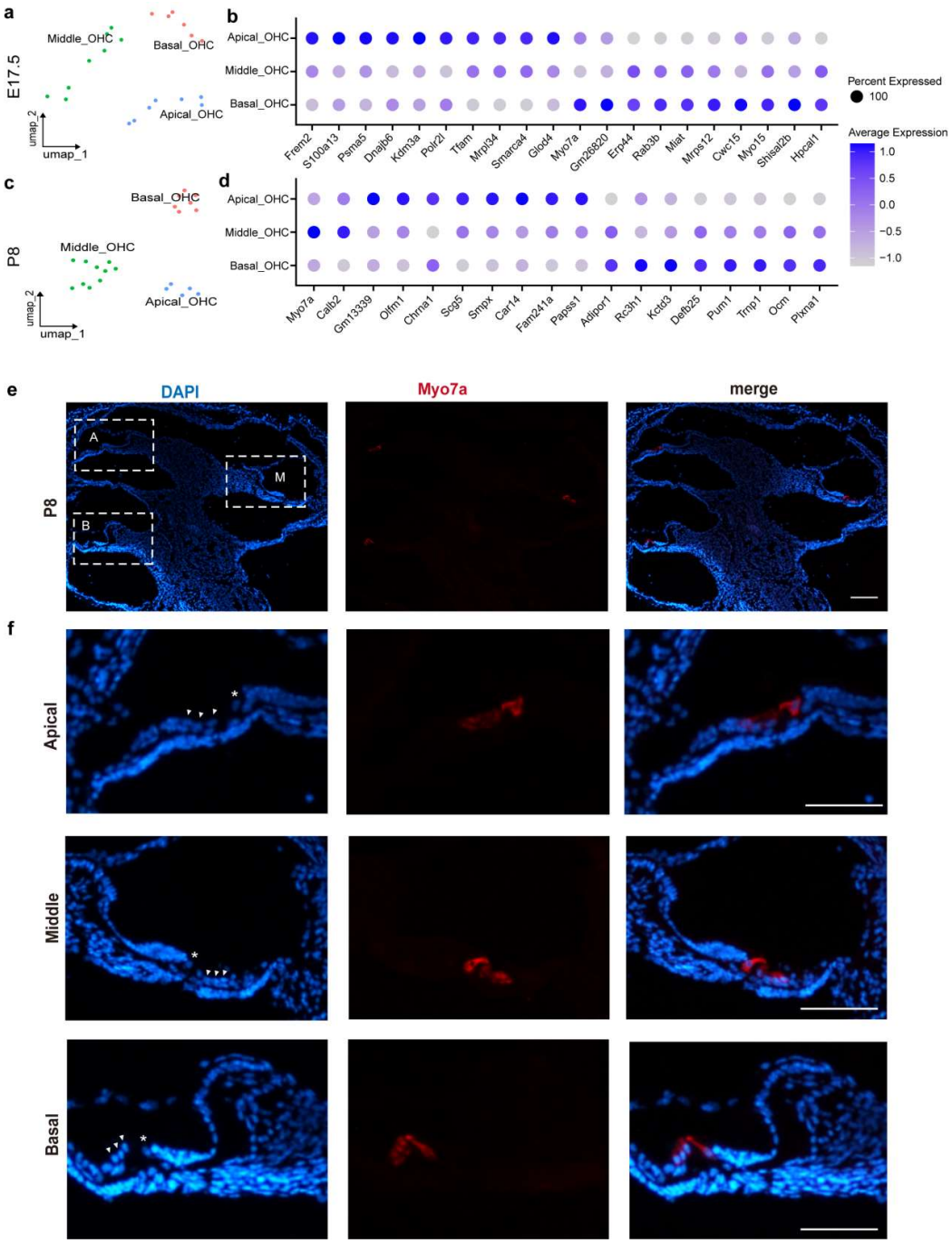

Fig. S6-1 Spatial differential analysis of OHC from apex to base. (**a**) UMAP plot showing OHCs extracted from apical, middle and basal regions of E17.5 cochlea. (**b**) Bubble plot showing the expression levels of a set of genes representing two gradient

patterns (apex-to-base decreasing and increasing expression) in OHCs from E17.5 cochlea. The size of the dots represents the percentage of cells in the clusters expressing the genes and the color intensity represents the average expression levels of the gene in that cluster. (**c**) UMAP plot showing OHCs extracted from apical, middle and basal regions of P8 cochlea. (**d**) Bubble plot showing the expression levels of a set of genes representing two gradient patterns (apex-to-base decreasing and increasing expression) in OHCs on P8 cochlea sections. (**e**) Immunostaining of Myo7a (red) on the P8 cross section. Dashed boxes indicated the apical, middle, and basal regions of the cochlea. DAPI is labeled in blue. Scale bars equal to 200 μm). (**f**) Magnified view of the dashed boxes in (**e**) to show the variant expression level of Myo7a in hair cells from apical (upper), middle (middle) and basal (bottom) regions, respectively. A, apical; M, middle; B, basal.

Figure S6-2

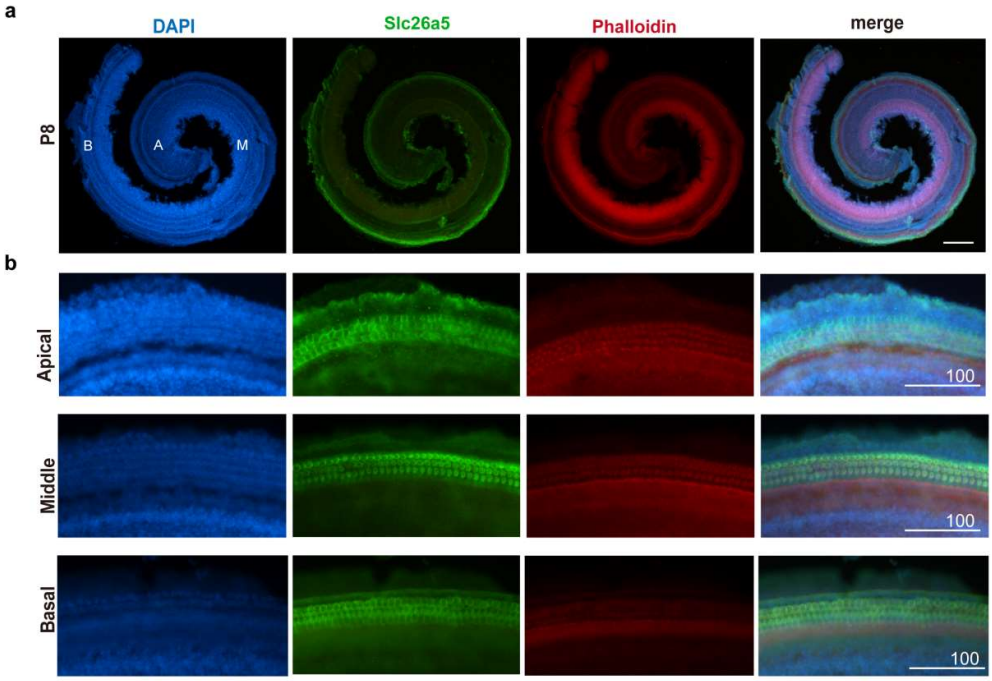

c

E17.5 Biological Process	log10(*P*-value)	P8 Biological Process	log10(*P*-value)	Adult Biological Process	log10(*P*-value)
Proteasome degradation	-4.18	inner ear receptor cell stereocilium organization	-6.03	hair cell differentiation	-4.36
Transcriptional regulation by RUNX1	-2.51	inner ear development	-3.91	epidermis development	-2.26
mitochondrial membrane organization	-3.22	epithelial cell differentiation	-2.13	locomotory behavior	-3.79
RNA splicing, via transesterification reactions	-2.25	Ion transport by P-type ATPases	-4.46	telencephalon development	-3.72
DNA-templated transcription	-2.05	kidney epithelium development	-3.87	cell morphogenesis	-2.98

d

E17.5 Biological Process	log10(*P*-value)	P8 Biological Process	log10(*P*-value)	Adult Biological Process	log10(*P*-value)
mitochondrial transport	-3.06	regulation of monoatomic anion transport	-4.98	clathrin-dependent endocytosis	-5.26
inner ear development	-2.75	Cardiac conduction	-2.91	synaptic vesicle recycling	-3.81
regulation of epithelial cell proliferation	-2.99	limbic system development	-2.63	actin filament organization	-5.17
kidney development	-2.30	positive regulation of cell development	-2.14	export from cell	-3.17
negative regulation of apoptotic pathway	-2.62	positive regulation of mRNA metabolic process	-2.48	neurotransmitter secretion	-2.27

Fig. S6-2 Spatial differential analysis of OHCs from apex to base. (**a**) Immunostaining of Slc26a5 (green), and phalloidin (red) in the P8 whole amount cochlea. DAPI is labeled in blue. (**b**) Magnified view of (**a**) to show spatial differential expression of Slc26a5 in apex (upper), middle (middle), and basal (bottom) regions, respectively. Scale bar equals to 200 μm. A, apical; M, middle; B, basal. (**c**,**d**) GO functional analysis of two classes of OHC gradient genes, with apex-to-base decreasing **(c)** and increasing expression pattern **(d)**, respectively**.**

Figure S7-1

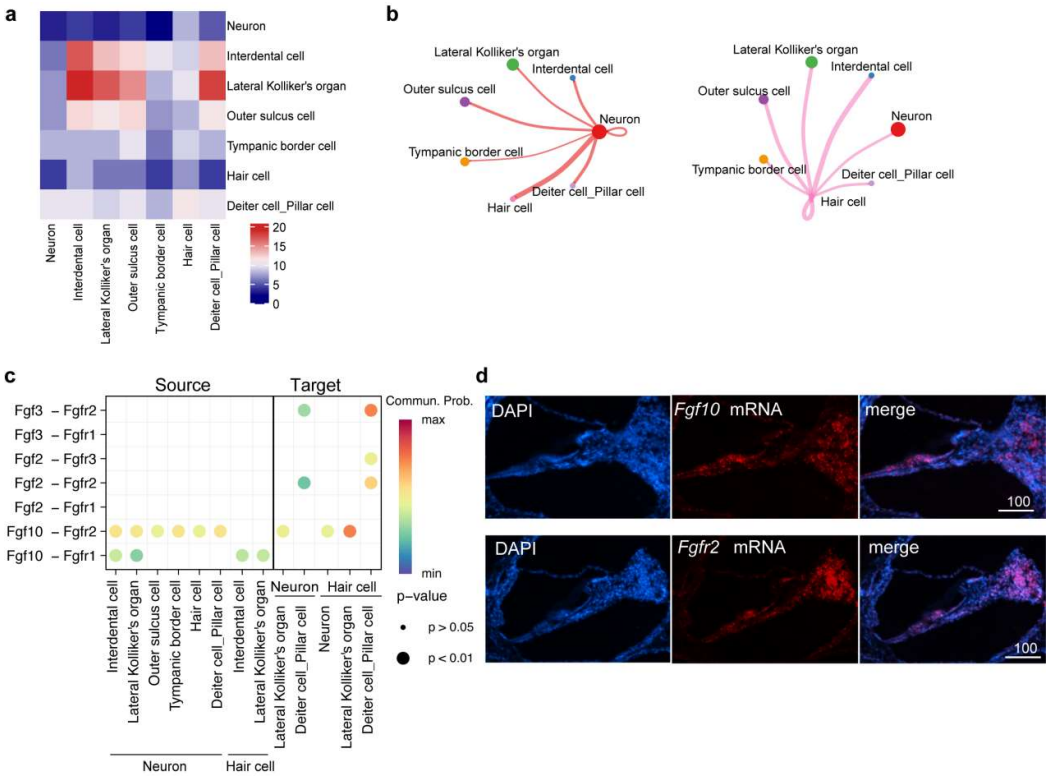

Fig. S7-1 Cell-cell communication network among neuron cell and cell clusters from Corti. (**a**) Heatmap showing the number of ligand-receptor pairs evaluated by cellchat for neuron cell and cell clusters from OC at E17.5 (**b**) Left, number of significant ligand-receptor pairs of neuron cells (hub) interacted with cell clusters from OC at E17.5. Right, number of significant ligand-receptor pairs between hair cells (hub) and neuron cells as well as other cell clusters from OC at E17.5. The edge width is proportional to the indicated number of ligand-receptor pairs. (**c**) Bubble plots showing ligand-receptor pairs of FGF signaling pathway between neuron cells and cell clusters from OC at E17.5. The size of dots represents the significance and the color represents the communication probability. (**d**) Magnified views of RNA *in situ* detection of *Fgf10* and *Fgfr2* mRNA in Fig. 7.

Figure S7-2

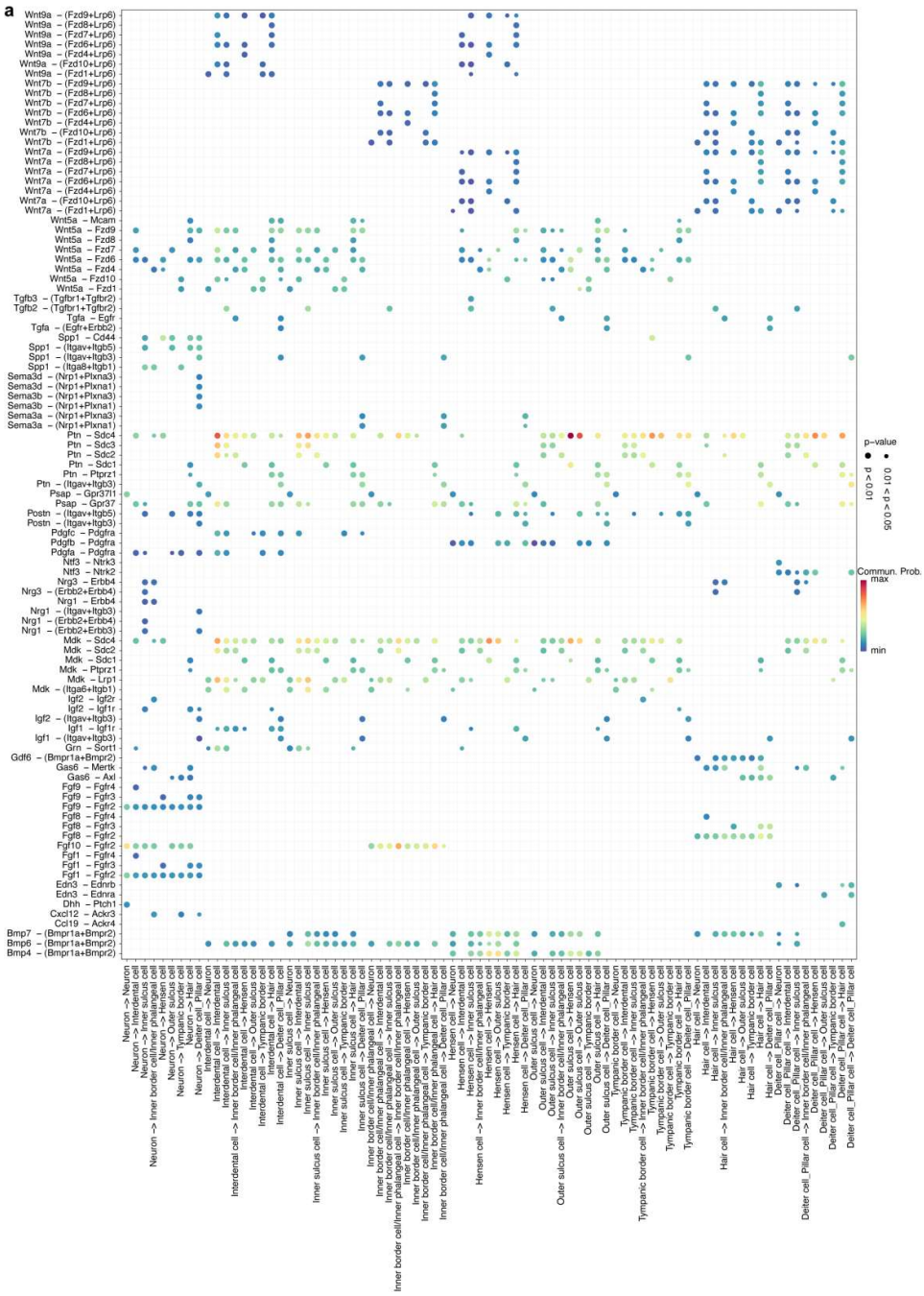

Fig. S7-2 Cell-cell communication network among neuron cell and cell clusters from the organ of Corti. Bubble plots showing ligand-receptor pairs between neuron cells and other cell clusters from the organ of Corti for the P8 spatial data. The size of

dots represents the significance and the color represents the communication probability.

Figure S8

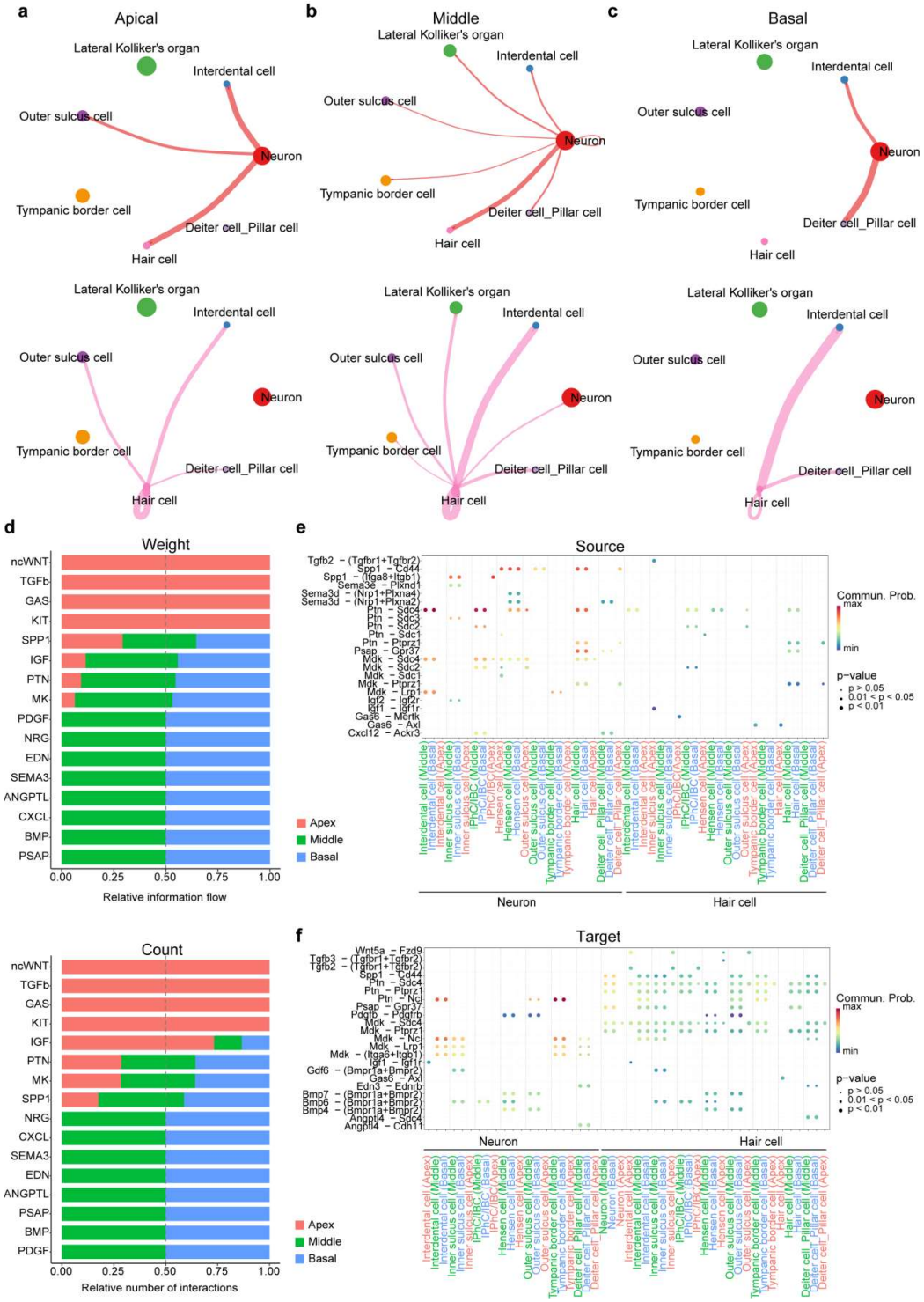

Fig. S8 Spatial cell-cell communication network among neuron cells and cell clusters from Corti. (a-c) Number of significant ligand-receptor pairs between neuron

cells and cell clusters from organ of Corti (OC) distributed in the apical (**a**), middle (**b**), and basal (**c**) regions at E17.5 stage, respectively. Up, the neurons are the hub; bottom, the hair cells are the hub. The edge width is proportional to the indicated number of ligand-receptor pairs. (**d**) Stack diagram comparing the weight (upper) and number (bottom) of interactions every signaling pathway predicted between neuron cells and cell clusters from OC distributed in the apical, middle and basal regions at E17.5 stage, respectively. (**e**) Bubble plots showing that neuron cells and hair cells are the source sending information to other cell clusters from OC in the different regions at E17.5 stage. The size of dots represents the significance and the color represents the communication probability. (**f**) Bubble plots showing the ligand-receptor pairs that neuron cells and hair cells are the targets to receive information from other cell clusters from OC in the different regions at E17.5 stage. The size of dots represents the significance and the color represents the communication probability.

Figure S9

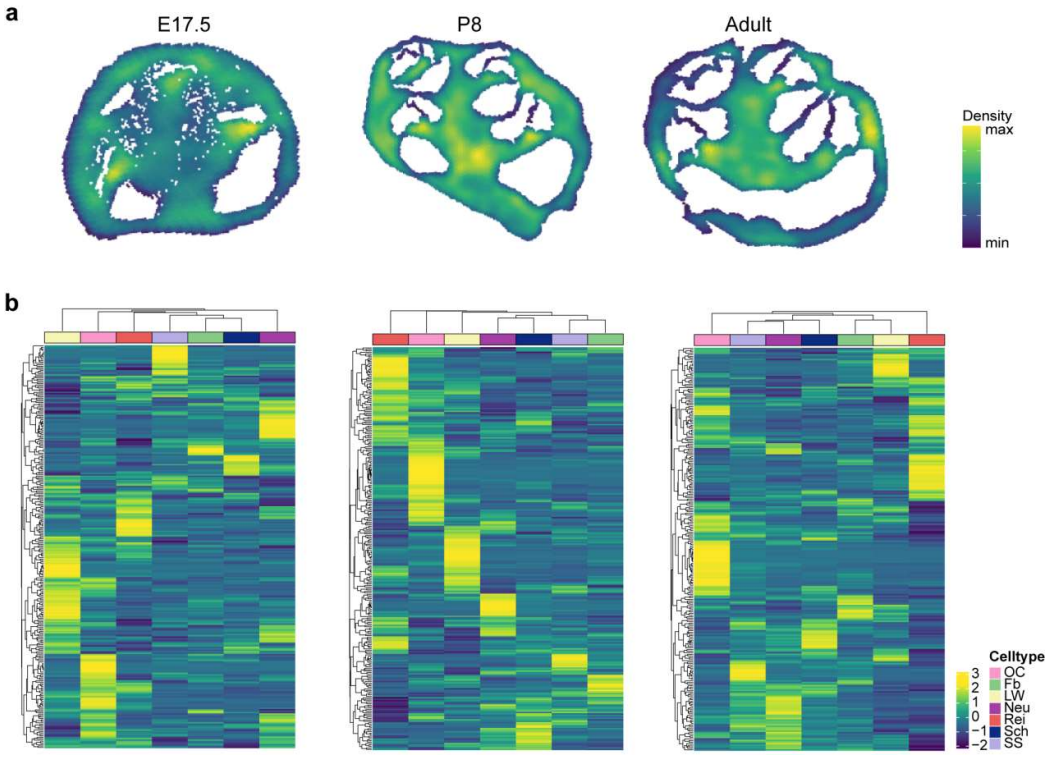

Fig. S9 Spatiotemporal expression pattern of known deafness genes (a) Density plots showing the spatial expression of all known deafness genes, on E17.5, P8 and Adult cochlea section. Strong densities were found at the organ of Corti (OC) region on E17.5 section, at OC and SGN region on P8 section, and at the central modiolus region on adult section. **(b)** Hierarchical clustering of cochlear cell types and deafness genes in spatiotemporal transcriptomic data. OC: the organ of Corti, Fb: fibrocytes, LW: lateral wall, Neu: neurons, Rei: reissner's membrane, Sch: Schwann cell, SS: surrounding structures.